

Submitted to ApJ

Identifying Lensing by Substructure. I. Cusp Lenses

Charles R. Keeton^{1,2}, B. Scott Gaudi^{1,3}, and A. O. Petters^{4,5}

ABSTRACT

The observed flux ratios of many 4-image gravitational lenses cannot be fit with standard smooth lens models. It has been argued that these anomalous flux ratios provide evidence for significant amounts of substructure in lens galaxies. However, that conclusion generally relies on detailed fitting of lens data, and is therefore model dependent and difficult to interpret. A potentially more straightforward and unambiguous method of identifying substructure is to appeal to generic, model-independent relations between images in certain configurations that are indicative of the source being near a caustic. For a triplet of images associated with an ideal cusp caustic, the sum of the signed magnifications should vanish; this relation can be violated only if there is significant structure in the lens potential on scales smaller than the image separations. However, this generic relation is strictly true only for an ideal cusp catastrophe. Real lenses will have magnifications that violate the relation purely because the caustics are not ideal cusps, complicating attempts to identify flux ratio anomalies. We quantify the degree to which the ideal cusp relation is violated for realistic lens models involving ellipticity, shear, and different radial profiles. We then use our results to identify flux ratio anomalies in observed lenses. We find that the cusp relation alone indicates that the cusp lenses RX J0911+0551 and B2045+265 have flux ratio anomalies at better than 99% confidence, while B0712+472 is marginally anomalous at the 95% level. Interestingly, the cusp relation does not reveal a significant anomaly in the cusp lens B1422+231, even though this lens is known to be anomalous from detailed modeling. Methods that are more sophisticated (and less robust) than the cusp relation may therefore be necessary to uncover flux ratio anomalies in some systems.

Subject headings: cosmology: theory — dark matter — galaxies: formation — gravitational lensing — large-scale structure of universe

¹Hubble Fellow

²Astronomy and Astrophysics Department, University of Chicago, 5640 S. Ellis Ave., Chicago, IL 60637; ckeeton@oddjob.uchicago.edu

³School of Natural Sciences, Institute for Advanced Study, Princeton, NJ 08540; gaudi@sns.ias.edu

⁴Department of Mathematics, Duke University, Durham, NC 27708; petters@math.duke.edu

⁵Bass Society of Fellows, Duke University

1. Introduction

The popular Cold Dark Matter (CDM) paradigm for cosmological structure formation has recently been facing something of a crisis, which may be summarized as an over-prediction of the amount of small-scale power (see, e.g., Spergel & Steinhart 2000 for a discussion). The problems fall into two main categories. First, the dark matter halos of real galaxies appear to be substantially less concentrated than predicted by CDM, as indicated by the rotation curves of supposedly dark matter dominated low surface brightness galaxies (e.g., Flores & Primack 1994; Moore 1994; de Blok, McGaugh & Rubin 2001; de Blok & Bosma 2002; but see, e.g., van den Bosch & Swaters 2001 for a dissenting view), the lifetimes and kinematics of bars in high surface brightness galaxies (Debattista & Sellwood 2000; Weiner, Sellwood & Williams 2001), strong gravitational lensing by elliptical galaxies (Keeton 2001a; Kochanek 2002b), and microlensing in the Milky Way (Binney & Evans 2001). Second, CDM simulations predict that a galaxy like the Milky Way should be surrounded by hundreds or even thousands of $\sim 10^7$ – $10^9 M_\odot$ satellites, whereas only a few dozen are observed (Klypin et al. 1999; Moore et al. 1999).

The extent of the crisis is still subject to debate. On the concentration problem, recent work has revealed discrepancies between different simulation methods (Weinberg & Katz 2001; Valenzuela & Klypin 2002; Sellwood 2002), which need to be resolved to verify or discount the CDM predictions. Even if the problem survives this examination, it might be solvable with relatively mundane explanations like a small tilt in the power spectrum (Zentner & Bullock 2002). On the substructure (satellite) problem, several recent studies have emphasized that the clumps of dark matter predicted by CDM are not necessarily the same as observable satellite galaxies (e.g., Stoehr et al. 2002; Hayashi et al. 2002). In particular, mass clumps will be visible only if they contain hot gas and/or stars, and astrophysical processes such as photoionization might easily produce a situation where most clumps are invisible (e.g., Bullock, Kravtsov & Weinberg 2000; Somerville 2002; Benson et al. 2002).

To further test the substructure problem, we must either find or rule out a population of dark clumps in galaxy halos. The observable effects of such clumps are surprisingly few; notably, the classic argument that they would heat stellar disks appears to be irrelevant for the mass functions expected for CDM (Font et al. 2001). One way that dark clumps can be detected, however, is with gravitational lensing.

Mao & Schneider (1998) first drew the connection between lensing and small-scale structure in galaxies. Many authors have been able to reproduce the image positions in 4-image lenses to milli-arcsecond accuracy with simple, smooth lens models, but have failed to reproduce the observed flux ratios (e.g., Kent & Falco 1988; Falco, Lehár & Shapiro 1997; Keeton, Kochanek & Seljak 1997).⁶ Until recently this flux ratio problem received little attention, perhaps because the number

⁶The problem is less apparent in 2-image lenses, mainly because the limited number of constraints leaves more freedom in the models.

of 4-image lenses was relatively small, and because it seemed possible to appeal to electromagnetic — non-gravitational — effects such as extinction by dust or scattering by hot gas. However, the number of lenses with apparently anomalous flux ratios is growing rapidly (P. Schechter, S. Burles, and N. Inada, private communication), and direct evidence suggests that, although electromagnetic effects do exist in observed lenses, they are not common (Falco et al. 1999; Winn et al. 2001, 2002). Mao & Schneider (1998) suggested that the flux ratio anomalies might be attributed to gravitational effects omitted from standard lens models, namely small-scale structure in the lens galaxy. More recently, several authors have noted that significant small-scale structure is exactly what is predicted by CDM, so there may be a natural connection between the substructure problem in CDM and the flux ratio problem in lensing that resolves both simultaneously. The amount of substructure predicted by CDM appears to be in nice agreement with the amount required by lensing (Metcalf & Madau 2001; Chiba 2002; Dalal & Kochanek 2002).

This preliminary agreement is tantalizing. However, given the potential importance of the result, each link in the chain of reasoning that leads from anomalous flux ratios to CDM substructure must be examined rigorously. In particular, how robust is the conclusion that realistic galaxies cannot reproduce the observed flux ratios if they lack substructure? Given the manner in which flux ratio anomalies are identified, this question can be conceptually divided into two parts. First, how robust is the conclusion that smooth lens models cannot reproduce the flux ratios? Second, how well (in the lensing sense) do these lens models approximate real galaxies? Even if the need for substructure in the lensing galaxies is firmly established, how confident are we that the required substructure is the type predicted by CDM, as opposed to stars, globular clusters, dwarf satellites, tidal streams, simple density perturbations, etc.? Several authors have addressed how this last question can be answered with various types of data (e.g., Metcalf & Madau 2001; Dalal & Kochanek 2002; Metcalf 2002; Moustakas & Metcalf 2002). Here we concentrate on the first link in the chain, namely the question of how well we can identify flux ratios that cannot be reproduced by smooth lens models.

As long as the identification of flux ratio anomalies relies on detailed modeling (see Metcalf & Zhao 2002 for a nice example), critics may argue that smooth models consistent with observed flux ratios have simply been overlooked, so there may in fact be no anomalies and no need for substructure. Fortunately, such criticism may be sidestepped. Strong, model-independent claims for anomalies can be made by invoking simple and generic relations between the image magnifications that should be satisfied for images in “fold” or “cusp” configurations (defined in §2).⁷ The magnification relations are derived from the local lensing properties and are independent of the global mass model, so they should be satisfied by *all* lenses in fold and cusp configurations. Violations of

⁷There are also global magnification relations (i.e., relations involving all four images) that hold for all image configurations, at least for certain families of lens potentials (Dalal 1998; Witt & Mao 2000; Dalal & Rabin 2001; Hunter & Evans 2001; Evans & Hunter 2002). Unfortunately, those relations cannot be written using only observable quantities; they all require knowledge of the intrinsic flux of the source. The global relations therefore cannot be used in a model-independent way.

the relations therefore indicate that *no* smooth model can reproduce the observed flux ratios, and there must be density fluctuations on scales smaller than the separations between the images (see Mao & Schneider 1998).

The magnification relations hold, however, only for ideal fold and cusp catastrophes. The caustics in real lens systems only approximate ideal folds and cusps in some low-order expansion of the potential near the critical point; higher-order terms introduce deviations from the fold and cusp geometries. Thus, real lens systems will only approximately obey the ideal magnification relations. The accuracy with which the relations hold will depend on the distance of the images from the critical point and on properties of the lens model, so it is not straightforward to judge *a priori* the significance of an observed flux ratio anomaly, even for apparent fold and cusp image configurations.

Our goal is to quantify the magnification relations in both ideal and realistic limits, and to express them in terms of lens observables. In this paper we focus on cusp configurations. Cusps are the highest order stable singularities in lensing maps (see Schneider, Ehlers & Falco 1992; Petters, Levine & Wambsganss 2001), a fact that simplifies the identification of cusp configurations⁸ and permits certain types of analytic work. We will address fold configurations in a subsequent paper (Gaudi, Keeton & Petters, in preparation). We study the cusp relation for several families of models that encompass both the range of expected properties of most lens galaxies, and also the range of mass models that have been used previously to fit the majority of lens systems and identify flux ratio anomalies. In particular, we consider models with ellipticity, external shear, and different radial density profiles. Using both analytic and numerical methods, we calculate the cusp relation in these models, and compare it to observed lensed systems. In this way we identify flux ratio anomalies that indicate a need for substructure without resorting to explicit modeling.

There is a semantic question that must be addressed here: Where should the line between a “smooth” lens model and “substructure” be drawn? One might argue that models that are only slightly more complicated than what we consider but still “smooth” — e.g., models with a boxy potential, like those studied by Evans & Witt (2001) and Zhao & Pronk (2001) — might be able to reproduce the observed flux ratios without invoking the granular substructure predicted by CDM. In general, what is needed to violate the cusp relation is significant power in the lens potential on angular scales of order the image separations. This condition can already be met in the models we consider; the singular isothermal ellipsoid has power in all even multipoles, with more power for larger ellipticities. Even such a simple model therefore admits significant deviations from the ideal cusp relation for sufficiently large ellipticities (as noted by Keeton & Kochanek 1998 in the context of spiral galaxy lensing). At this point, considering effects beyond ellipticity, shear, and radial profiles would increase the complexity of the analysis without offering much additional insight. Ultimately, one would like to adopt a more fully model-independent approach, such as

⁸A close triplet of images always indicates a cusp configuration; but a close pair of images could be associated with either a fold or a cusp.

representing the lenses as a superposition of multipoles and determining the amount of power in various multipoles required to fit the observed flux ratios. We leave that as an interesting topic for future study.

The layout of the paper is as follows. We begin in §2 by reviewing 4-image lensing and introducing a way to characterize the image configurations quantitatively. In §3 we discuss cusp image configurations and present the generic, universal relation that should be obeyed by the image magnifications for sources near an ideal cusp. We then test this ideal relation, first using analytic results for simple lens models (§4), and then with Monte Carlo simulations of realistic lens populations (§5). In §6 we apply the cusp relation to observed lenses, using violations of the relation to identify lenses that require substructure. We offer our conclusions in §7. Several appendices present supporting technical material. In Appendix A we derive the universal relations between the positions and magnifications of sources near an ideal cusp. In Appendix B we obtain exact analytic solutions of the lens equation for two families of simple lens models, which can be used to obtain exact analytic expressions for the realistic cusp relations. And in Appendix C we explore the cusp image position relations for the simple lens models. Throughout this paper we consider only 4-image systems, and we ignore faint fifth images that may appear near the centers of the lens galaxies.⁹

2. Characterizing 4-Image Lenses

To date, seventeen 4-image lens systems have appeared in the literature. (See Turner, Keeton & Kochanek 2002 for a summary and list of references.) This count includes only systems that have exactly four images of a given source, and where the images appear point-like at some wavelength. It includes the 10-image system B1933+503, which is complex only because there are three distinct sources; none of the sources has an image multiplicity larger than four (Sykes et al. 1998). By contrast, it excludes PMN J0134–0931 and B1359+154, because they have multiplicities larger than four due to the presence of multiple lens galaxies (Rusin et al. 2001; Winn et al. 2002; Hall et al. 2002). One other lens, 0047–2808, is almost certainly quadruply-imaged as well (Warren et al. 1996, 1999; Koopmans & Treu 2002), but its lack of point-like images makes it difficult to analyze with the usual techniques used for point-like systems.

Quadruple imaging requires a lens potential that is not axially symmetric. (See the monographs by Schneider et al. 1992 and Petters et al. 2001 for a review of lens theory.) The symmetry is typically broken by asphericity in the lens galaxy mass distribution or by a gravitational tidal shear from another object near the lens galaxy. The region in the source plane that corresponds to 4-image lenses is bounded by an astroid-shaped caustic consisting of four cusps connected by four fold lines

⁹Fifth images have not been detected, and they are predicted to depend only on the densities of lens galaxies at very small radii, so they are irrelevant for our purposes. Still, they are interesting in their own right, as discussed recently by Keeton (2002a).

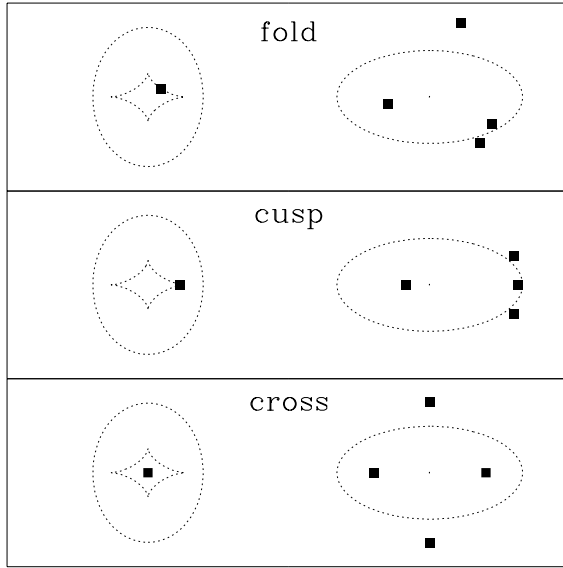


Fig. 1.— The three basic configurations of 4-image lenses: fold (top), cusp (middle), and cross (bottom). In each panel, the figure on the left shows the caustics and source position in the light source plane, while the figure on the right show the critical curves and image positions in the image plane.

(see Figure 1). The properties of the caustic can be studied with mathematical catastrophe theory and described in terms of the fold and cusp catastrophes, which produce characteristic distortions and image configurations.

The fold and cusp image configurations have, respectively, two and three images close together, are shown in Figure 1. Also shown is the third common configuration, the cross, characterized by a relatively symmetric morphology produced by a source that is not close to the caustic. It is usually easy to categorize an observed lens as a fold, cusp, or cross. Nevertheless, the categories actually blend into each other with no sharp boundaries, so we would like to develop a formal method of characterizing image configurations. Given our focus on cusps configurations characterized by a close triplet of images, we introduce two quantities as follows. For a given 4-image lens, pick a triplet of images; two examples of triplets in RX J0911+0551 are shown in Figure 2. Let d be the maximum separation between the three images in the triplet, and let θ be the opening angle of the polygon spanned by the images, measured from the position of the lens galaxy. Each 4-image lens has four distinct triplets and hence four values of θ and d . We can identify image triplets associated with cusps as those where θ and/or d is small. Even though there is no rigorous definition of when θ and d are “small” enough to indicate a cusp, we will see below that these are useful quantities for characterizing the range of image configurations.

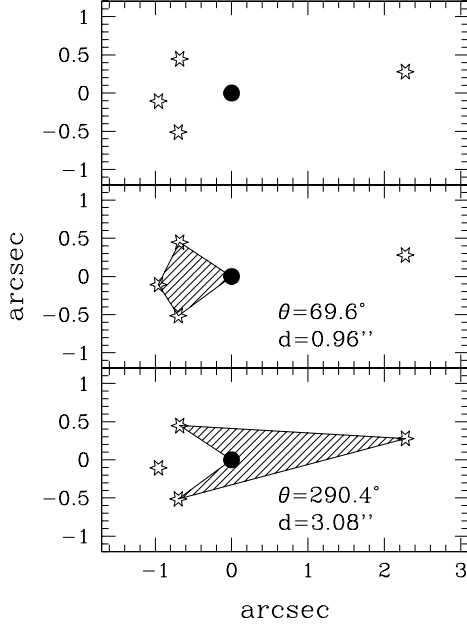


Fig. 2.— The top panel shows the positions of the images (stars) and lens galaxy (filled circle) for RX J0911+0551 (Burud et al. 1998). The middle and bottom panels show two of the four different image triplets, with the opening angle θ and separation d indicated.

3. Universal Magnification Relation for Cusps

In this section we briefly review the lensing of a source close to and inside an ideal cusp and present the magnification relation used in the subsequent analysis. Appendix A discusses lensing near a cusp in considerably more detail, and presents additional position and magnification relations for cusp images.

In the vicinity of a cusp, the lens equation relating the source position \mathbf{u} to the image position $\boldsymbol{\theta}$ can be written to third order in $\boldsymbol{\theta}$ as a polynomial mapping,

$$u_1 = c \theta_1 + \frac{b}{2} \theta_2^2, \quad u_2 = b \theta_1 \theta_2 + a \theta_2^3. \quad (1)$$

The coordinates \mathbf{u} and $\boldsymbol{\theta}$ are local orthogonal coordinates that are related to the global coordinates \mathbf{y} and \mathbf{x} of the lens system by $\mathbf{u} \equiv M\mathbf{y}$ and $\boldsymbol{\theta} \equiv M\mathbf{x}$. The transformation matrix M depends on the lens potential. For the simple analytic models we consider in §4 and Appendix B, the transformation matrix M is the identity matrix and the $\boldsymbol{\theta}$ and \mathbf{u} coordinate systems are simply the \mathbf{x} and \mathbf{y} coordinate systems translated so the cusp point is at the origin. The constant coefficients a, b and c are given by derivatives of the potential at the critical point (see eq. A6 in Appendix A).

Solving for θ_1 in the left-hand side of eq. (1) and substituting into the right-hand side, one obtains a cubic equation for θ_2 that depends on a, b, c and the source position \mathbf{u} . Inside the caus-

tic, there are three real solutions to this cubic equation, and thus three images of the source. It is possible to derive six independent relations between the positions and magnifications of these images. Unfortunately, only one of these relations can be recast to depend only on directly observable properties: the well-known magnification sum rule (Schneider & Weiss 1992; Zakharov 1995; Petters et al. 2001, p. 339),

$$\mu_1 + \mu_2 + \mu_3 = 0, \quad (2)$$

where the μ_i are the signed magnifications of the three images. The other relations depends on properties that are not directly observable, such as the position of the source or the mapping coefficients a, b, c .

4. The Cusp Relations in Simple Lens Models

The ideal cusp relation eq. (2) relies on the assumption that the lensing map has the polynomial form given in eq. (1). In general this form is just an approximation to the true lensing map, obtained for example from a Taylor series expansion near the cusp point. Thus, we expect the cusp relation to hold rigorously only when the source is asymptotically close to the cusp. In this section we begin to quantify the deviation from the ideal cusp relation that arises because the lensing map eq. (1) is only an approximation, using simple lens models to illustrate the effects of ellipticity, shear, and different radial profiles.

Although the magnifications appearing in the cusp relation eq. (2), are not directly observable, we can follow Mao & Schneider (1998) and divide out the unknown source flux by defining the dimensionless quantity

$$R_{\text{cusp}} \equiv \frac{\mu_1 + \mu_2 + \mu_3}{|\mu_1| + |\mu_2| + |\mu_3|} = \frac{F_1 + F_2 + F_3}{|F_1| + |F_2| + |F_3|}, \quad (3)$$

where the μ_i are the magnifications and the F_i the observed fluxes, both with signs indicating the image parities. The parities can be determined unambiguously because in any triplet of adjacent images, the two outer images have the same parity while the middle image has the opposite parity (see Schneider et al. 1992; Petters et al. 2001). The expected cusp relation then has the form $R_{\text{cusp}} = 0$.

We first study the cusp relation analytically using two families of lens models where we can obtain exact solutions of the lens equation: a galaxy with a surface mass density of the form $\Sigma \propto r^{2-\alpha}$ with an external shear γ ; and a singular isothermal ellipsoid with an external shear γ aligned with the minor or major axis of the galaxy. Appendix B describes these models in detail and provides exact solutions to the image positions and magnifications for sources on the two symmetry axes of the lens potential.

Using these exact solutions we can obtain analytic expressions for R_{cusp} . For the power law galaxy plus shear models, when $\alpha = 1$ the galaxy is a singular isothermal sphere (SIS) and on-axis

sources have

$$R_{\text{cusp}} = -\frac{(1-\gamma)[1+\gamma(5-u_1)]u_1}{2\gamma(4+2u_1-u_1^2)+\gamma^2(8-5u_1+u_1^2)+u_1(1+u_1)}, \quad (4)$$

$$= \frac{2[1+3\gamma+2\gamma\cos(\theta/2)]\sin^2(\theta/4)}{3+2\gamma+(1+\gamma)\cos(\theta/2)+\gamma\cos\theta}, \quad (5)$$

$$= \frac{8(1+\gamma)}{6+4\gamma+(1+\gamma)\sqrt{4-(1-\gamma)^2(d/R_{\text{ein}})^2}+\gamma[2-(1-\gamma)^2(d/R_{\text{ein}})^2]} - 1, \quad (6)$$

where we have explicitly written the dependence on the (unobservable) source position u_1 as well as the (observable) opening angle θ and separation d of the image triplet. The separation appears via the dimensionless ratio d/R_{ein} , where R_{ein} is the Einstein ring radius of the lens. For power law models with other values of α , the expression for R_{cusp} can be written down but is complicated, so it makes sense just to examine the leading behavior. In terms of θ , we have:

$$\alpha = 0 : \quad R_{\text{cusp}} = \frac{1+4\gamma-\gamma^2}{32} \theta^2 + \mathcal{O}(\theta^4), \quad (7)$$

$$\alpha = 1 : \quad R_{\text{cusp}} = \frac{1+5\gamma}{32(1+\gamma)} \theta^2 + \mathcal{O}(\theta^4), \quad (8)$$

$$\alpha = \frac{3}{2} : \quad R_{\text{cusp}} = \frac{1+10\gamma+29\gamma^2}{32(1+3\gamma)^2} \theta^2 + \mathcal{O}(\theta^4). \quad (9)$$

These expressions can be converted to d using the relation

$$\frac{d}{R_{\text{ein}}} = \frac{2\sin(\theta/2)}{(1-\gamma)^{1/(2-\alpha)}}. \quad (10)$$

For the isothermal ellipsoid plus aligned shear model, the expression for R_{cusp} is again complicated so we examine the leading behavior,

$$R_{\text{cusp}} = \frac{15\gamma(1+5\gamma)+5\varepsilon(1+6\gamma-19\gamma^2)+\varepsilon^2(13-9\gamma+38\gamma^2)}{160(1-\varepsilon)(1+\gamma)[3\gamma+\varepsilon(1-2\gamma)]} \theta^2 + \mathcal{O}(\theta^4), \quad (11)$$

where ε is a convenient ellipticity parameter related to the axis ratio q by $\varepsilon = (1-q^2)/(1+q^2)$, so it is slightly different from the usual ellipticity $e = 1-q$ (see Appendix B.2). Note that eq. (11) reduces to eq. (8) for $\varepsilon \rightarrow 0$. To convert between θ and d , we have

$$\frac{d}{R'_{\text{ein}}} = \frac{1}{1-\gamma} \sqrt{\frac{2}{\varepsilon}} \tanh^{-1} \left[\frac{\sqrt{2\varepsilon} \sin(\theta/2)}{\sqrt{1-\varepsilon} \cos\theta} \right], \quad (12)$$

where R'_{ein} is a convenient parameter closely related to the Einstein ring radius (see Appendix B.2).

These results show that the cusp magnification relation is violated with an error that is second order in θ and d . The coefficients reveal how the error depends on the parameters. For a typical shear $\gamma \simeq 0.05$, radically changing the profile from $\alpha = 1$ (isothermal) to $\alpha = 0$ (point mass) changes

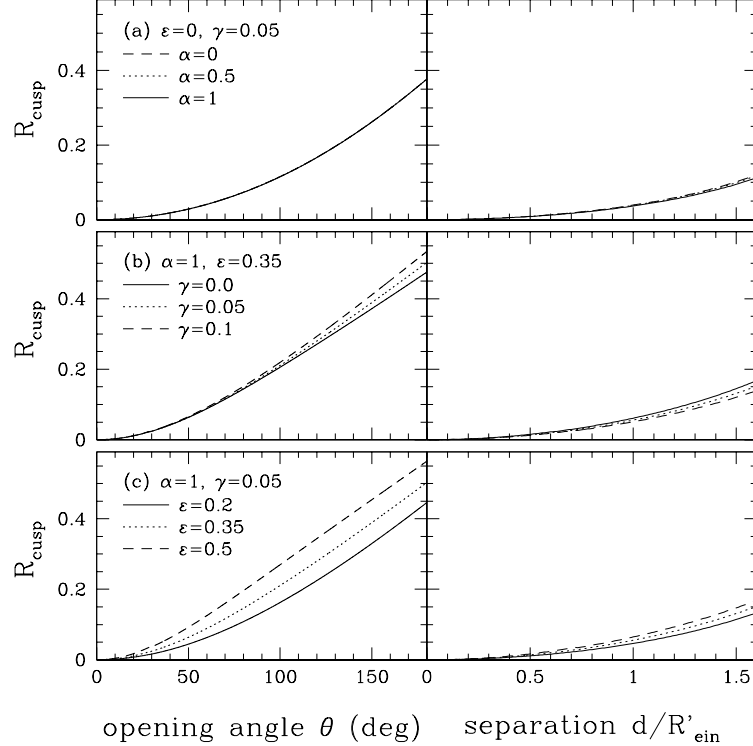


Fig. 3.— The cusp relation residual R_{cusp} as a function of the opening angle θ and the separation d of an image triplet, plotted for various lens models using the analytic solutions to the lens equation for sources on the major axis of the lens.

R_{cusp} by only 0.6% for fixed θ and 6% for fixed d . For isothermal models with typical values of the shear and ellipticity ($\gamma \simeq 0.05$ and $\varepsilon \simeq 0.35$; see §5), moderate changes in the shear of $\Delta\gamma = \pm 0.05$ affect R_{cusp} by $\sim 10\%$, while moderate changes in the ellipticity of $\Delta\varepsilon = \pm 0.15$ affect R_{cusp} by $\sim 20\%$ (both for fixed d). These dependences can also be seen in Figure 3, where R_{cusp} is plotted versus θ and d for various values of the parameters, using the full analytic expressions (not just the series expansions). We conclude that R_{cusp} is quite sensitive to ellipticity, moderately sensitive to shear, and not very sensitive to the density profile. This makes sense, because changing R_{cusp} requires changing the magnifications of images that are close together, which is best accomplished by changing the angular structure of the potential (ε and γ); modifying the density profile has little effect because the images lie at similar radii.

Figure 4 shows the dependences on ε and γ in more detail, including cusps on both the major and minor axes of the lens potential for both aligned and anti-aligned shears. (In this figure, the separation is held fixed at $d/R'_{\text{ein}} = 1$.) The dependences are complicated, partly because major and minor axis cusps are simply different, and partly because of the possibility of swallowtail caustics when the shear is anti-aligned (see Appendix B.2), but several points can be made. First, for major axis cusps and aligned shear, increasing the shear amplitude actually decreases R_{cusp} .

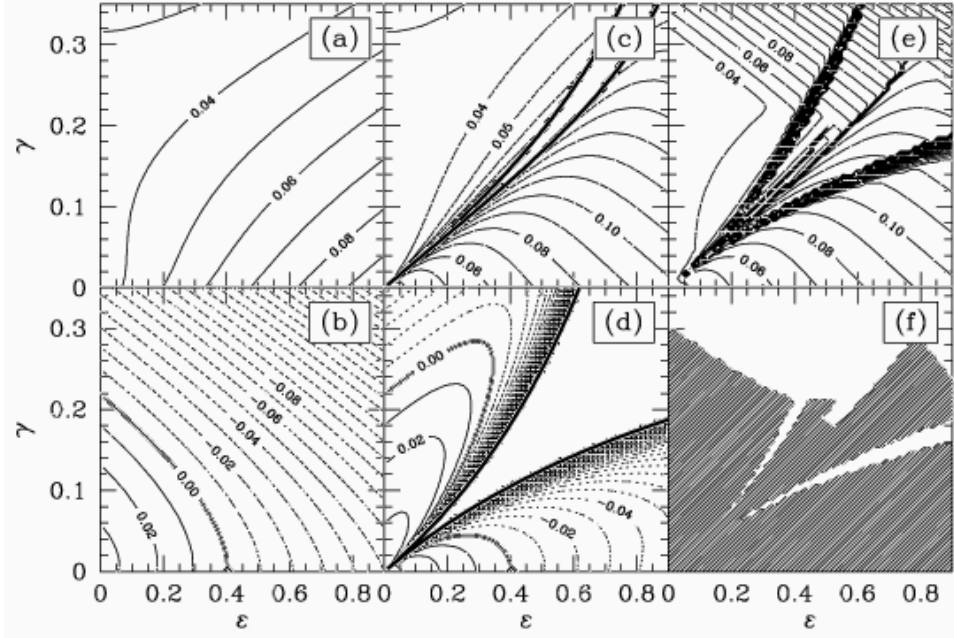


Fig. 4.— Panels (a)–(d) show contours of R_{cusp} versus ε and γ for fixed $d/R'_{\text{ein}} = 1$, plotted for the four possible cases as follows. (a) Aligned shear, major axis cusp. (b) Aligned shear, minor axis cusp. (c) Anti-aligned shear, major axis cusp. (d) Anti-aligned shear, minor axis cusp. The contours are spaced by $\Delta R_{\text{cusp}} = 0.01$; the heavy contour has $R_{\text{cusp}} = 0$, the light solid contours have $R_{\text{cusp}} > 0$, and the dashed contours have $R_{\text{cusp}} < 0$. In panels (c) and (d) results are omitted in the region of parameter space where the analytic formalism is invalid because the caustics have swallowtails (see Appendix B.2, especially eq. B21). Panel (e) shows contours of the *maximum* value of $|R_{\text{cusp}}|$ among the four cases. In panel (f), the shaded area shows the region of parameter space where $\max(|R_{\text{cusp}}|)$ occurs for a major axis cusp; in the rest of parameter space the maximum occurs for a minor axis cusp.

Second, minor axis cusps are generally more sensitive to the parameters than major axis cusps. Third, it is interesting to see that for minor axis cusps there are combinations of parameters where R_{cusp} vanishes even for a triplet with a large separation $d/R'_{\text{ein}} = 1$. Fourth, when we look at the maximum possible value of $|R_{\text{cusp}}|$ at each point in parameter space (Figure 4e) we see that in general it increases with both ellipticity and shear, but at small ellipticities it is fairly insensitive to the shear. Finally, and perhaps most importantly, Figure 4f show that when $\gamma \lesssim 0.2$ the maximum value of $|R_{\text{cusp}}|$ occurs for a major axis cusp.¹⁰

The analytic approach we have used so far is available only for sources on a symmetry axis

¹⁰Except for a narrow range of parameter space where swallowtail caustics are important; but models with swallowtails have very small cross sections for 4-image lenses, so they are of little practical importance (see Keeton, Mao & Witt 2000).

of the lens. To consider off-axis sources, we turn to Monte Carlo simulations. We pick random source positions and solve the lens equation (using the algorithm and software by Keeton 2001b) to generate a catalog of mock lenses. For each 4-image system we compute θ , d , and R_{cusp} for the four different image triplets. We then make a scatter plot of R_{cusp} versus θ and d , as shown in Figure 5. We repeat the analysis for a variety of lens models to see how the distribution for R_{cusp} depends on the model properties. In general, we see that the deviation of R_{cusp} from zero is small when the source is close to the cusp and θ and d are small, and grows as the source moves away from the cusp and θ and d increase. Beyond $\theta \sim 180^\circ$ and $d/R'_{\text{ein}} \sim 1.7$, the R_{cusp} distribution becomes more complicated because we have moved into a regime of image triplets that are manifestly not associated with cusps (see the bottom panel of Figure 2). The break at $d/R'_{\text{ein}} \sim 1.7$ is actually easy to understand. This is the separation for an image triplet corresponding to an equilateral triangle inscribed within the Einstein ring; when the separation is larger than this value, the images are so spread out that they are in no way associated with a cusp.

The Monte Carlo simulations reveal an intriguing and important result: for $\theta \lesssim 180^\circ$ and $d/R'_{\text{ein}} \lesssim 1.7$ (the entire region of interest for the cusp analysis) there is a firm upper envelope on the values of R_{cusp} . In fact there are two envelopes: one each for major and minor axis cusps. Moreover, if the lens has a symmetry axis, the envelope corresponds to the analytic predictions for sources on that axis. We can understand why the symmetry axis provides an upper envelope by examining derivatives of R_{cusp} with respect to the perpendicular distance u_2 from the axis. The first derivative vanishes by symmetry,

$$\frac{\partial R_{\text{cusp}}}{\partial u_2} \Big|_{u_2=0} = 0, \quad (13)$$

so the axis is a local extremum. The second derivative, which determines whether it is a local maximum or minimum, can be computed explicitly for an SIS plus shear model. After lengthy but straightforward algebra, we obtain

$$\begin{aligned} \frac{\partial^2 R_{\text{cusp}}}{\partial u_2^2} \Big|_{u_2=0} &= - \frac{(1+\gamma)^2}{\gamma^2 \sin^4(\theta/2) [3 + 2\gamma + (1+\gamma) \cos(\theta/2) + \gamma \cos \theta]^2} \\ &\times \left[4\gamma(1-\gamma) + (7 + 6\gamma - \gamma^2) \cos(\theta/2) + 16\gamma(2+\gamma) \cos^2(\theta/2) \right. \\ &\quad \left. + (5 + 18\gamma + 13\gamma^2) \cos^3(\theta/2) + 12\gamma(1+3\gamma) \cos^4(\theta/2) \right]. \end{aligned} \quad (14)$$

The factor on the first line is manifestly negative, while the quantity in square brackets on the second and third lines is positive over the entire interesting range $0 < \theta < \pi$ and $|\gamma| < 1$. Thus, the second derivative is negative, and hence R_{cusp} is a maximum on the axis. While this proof formally holds only for the SIS plus shear model, intuition and the Monte Carlo simulations suggest that it is not restricted to this model. Thus, the analytic results for on-axis sources provide a simple and important upper bound on R_{cusp} . When $\gamma \lesssim 0.2$ the bound comes from major axis cusps (see Figure 4f).

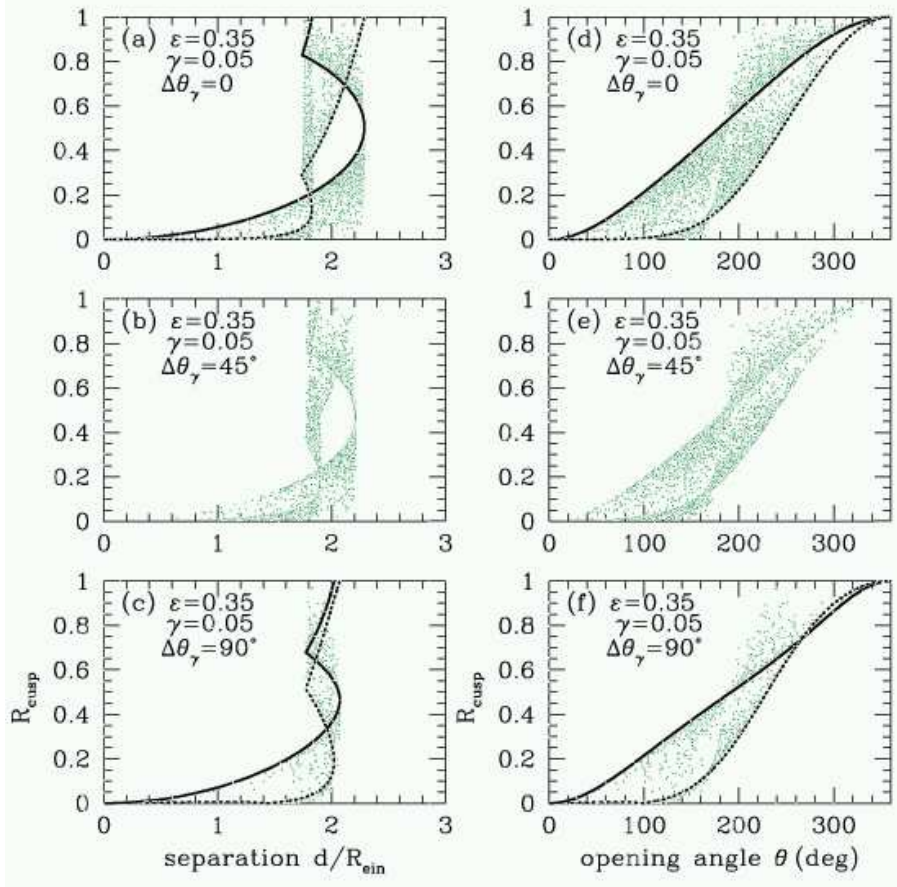


Fig. 5.— R_{cusp} versus θ and d , for various values of the ellipticity and shear and the angle $\Delta\theta_\gamma$ between them. The points show results for Monte Carlo simulations of random source positions. The heavy curves show the analytic results for on-axis sources, where solid (dotted) curves indicate the major (minor) axis of the lens potential. Analytic results are available only for $\Delta\theta_\gamma = 0$ and 90° .

To summarize, the ideal cusp relations break down in practice (for sources a small but finite distance from the cusp), but in a way that can be quantified. In general, $R_{\text{cusp}} \propto \theta^2 \propto d^2$ for small θ and d , and R_{cusp} grows slowly until at $d/R_{\text{ein}} \sim 1.7$ we reach triplets that are definitely not associated with cusps and the predicted cusp relation breaks down. The cusp relation is mainly sensitive to the angular structure of the lens potential (the ellipticity and shear), and is not very sensitive to the radial profile of the lens galaxy. If the cusp has a symmetry axis, sources on the axis provide a strict upper bound on R_{cusp} over the entire interesting range of θ and d . The lens equation can often be solved exactly for such sources to obtain simple, but important, analytic upper bounds on R_{cusp} .

5. The Cusp Relation in Realistic Lens Populations

The ellipticity and shear are the key quantities for the realistic (non-ideal) cusp relation, but we do not know them *a priori* for any observed lens. The mass ellipticity relevant for lensing cannot simply be inferred from the observed ellipticity of the light, because the two are not strongly correlated in individual lenses (Keeton, Kochanek & Falco 1998). The ellipticity and shear can be constrained with lens models (e.g., Keeton et al. 1997), but we seek to avoid explicit modeling if possible. To avoid these problems, we use Monte Carlo simulations of a realistic population of lenses to derive the probability distribution for R_{cusp} .

Specifically, we extend the Monte Carlo simulations introduced in §4 by drawing lenses from a population with realistic distributions of ellipticity and shear. We adopt the *light* ellipticity¹¹ distribution of E and S0 galaxies from the sample of Jørgensen, Franx & Kjærgaard (1995), which includes 379 galaxies from 11 clusters, including Coma. Even if mass and light ellipticities are not correlated on a case-by-case basis, it seems likely that their distributions are the same or similar; see Rusin & Tegmark (2001) for a discussion. The distribution has mean $\bar{e} = 0.31$ and dispersion $\sigma_e = 0.18$, and there are no galaxies with $e \gtrsim 0.8$. We use only isothermal ellipsoid lens galaxies, because as we argued in §4 the radial profile of the lens galaxy does not significantly affect the cusp relation. The galaxy mass is unimportant, because it simply sets a length scale (the Einstein radius) that can be scaled out by using the dimensionless separation d/R_{ein} .

We adopt a lognormal shear distribution with median $\gamma = 0.05$ and dispersion $\sigma_\gamma = 0.2$ dex. This is consistent with the distribution of shears expected from the environments of early-type galaxies, as estimated from N -body and semi-analytic simulations of galaxy formation (Holder & Schechter 2002). It is broadly consistent with the empirical distribution of shears required to fit observed lenses, at least when selection biases related to the lensing cross section and magnification bias are taken into account (see Holder & Schechter 2002). The mean shear is also consistent with the typical value needed to explain misalignments between the light and mass in observed lenses (Kochanek 2002a).

We draw 2000 sample lens potentials from these ellipticity and shear distributions, assuming random orientations for the shear and ellipticity axes. For each potential, we pick random sources with a number density of $\sim 10^3 R_{\text{ein}}^{-2}$ and solve the lens equation using the algorithm and software by Keeton (2001b). In this way we build up a set of mock lenses corresponding to a realistic population of galaxies. To determine how well the set of mock lenses should correspond to any real sample of lenses, we must consider two selection effects. First, the cross section for 4-image lenses is very sensitive to ellipticity and shear. Our uniform sampling of the source plane ensures that each lens

¹¹The ellipticities were determined from profile fitting to Gunn r photometry. Note that they are true ellipticities in the sense $e = 1 - q$ where q is the axis ratio, which differ slightly from the parameter ε used in the analytic formalism (see Appendix B.2), and we are careful to translate between them correctly. For example, the mean ellipticity $e = 0.31$ corresponds to $\varepsilon = 0.35$.

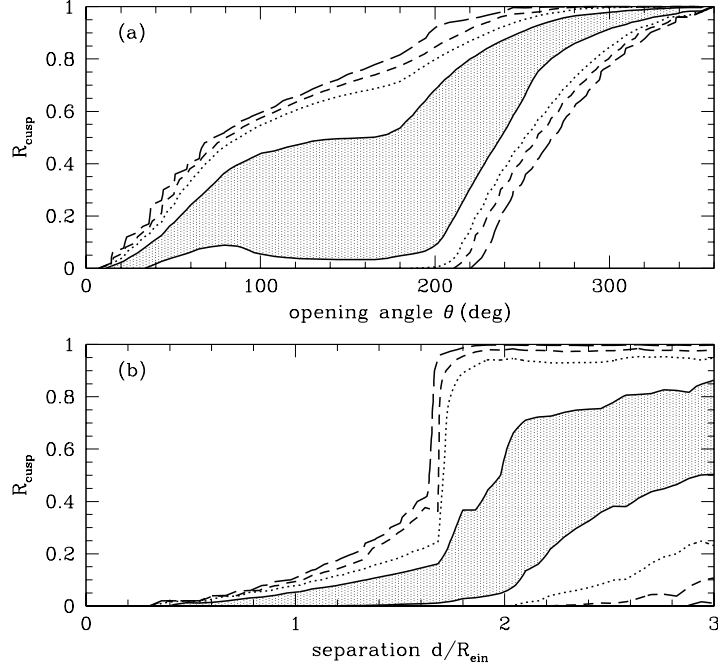


Fig. 6.— Contours of constant conditional probability $p(R_{\text{cusp}}|\theta)$ (top) and $p(R_{\text{cusp}}|d)$ (bottom), from the Monte Carlo simulations of a realistic lens population. The contours are drawn at the following confidence levels: 68% (solid), 95% (dotted), 99% (dashed), and 99.9% (long-dashed). Thus, in our set of mock lenses 68% of all image triplets lie in the shaded region between the solid curves, 99.9% of all triplets lie between the long-dashed curves, etc.

potential is automatically weighted by the correct cross section. Second, magnification bias can favor lenses with higher net amplifications, which can be important when comparing 4-image lenses to 2-image lenses (e.g., Keeton et al. 1997; Rusin & Tegmark 2001). However, this effect is likely to be less important when comparing different 4-image lenses against each other. If anything, it would favor the sources very near a cusp or fold that yield the highest magnification lenses that best satisfy the cusp/fold relations, giving more weight to lenses with *smaller* deviations from the ideal cusp/fold relations. We therefore neglect magnification bias and believe that this is a conservative approach.

For each 4-image lens, we identify the four different image triplets and compute θ , d , and R_{cusp} for each. We use the ensemble of these values to determine the conditional probability distributions $p(R_{\text{cusp}}|\theta)$ and $p(R_{\text{cusp}}|d)$, i.e. the probability of drawing a value of R_{cusp} given θ or d . We then paste all of the θ and d slices together to plot conditional probability contours as a function of θ and d , as shown in Figure 6. This figure is basically a modified version of Figure 5 where we have averaged over appropriate distributions of ellipticity and shear.

This figure is the culmination of our theoretical effort, so let us explain it carefully. In our set of mock lenses, 68% of all image triplets at fixed d/R_{ein} or θ lie in the shaded region between the solid curves, 99.9% of all triplets lie between the long-dashed curves, and so forth. If our Monte Carlo simulations reasonably represent the population of lens galaxies, and if lens galaxies have smooth mass distributions, then an observed lens should have a 68% probability of having a value of R_{cusp} that lies between the solid curves, a 99.9% probability of having a value of R_{cusp} between the long-dashed curves, and so forth. An observed lens lying outside of the contours would indicate, with high confidence, that one of the two assumptions is invalid for this lens. Since we believe that our simulations include a reasonable distribution of galaxy properties, we believe that any lens lying outside the contours represents a flux ratio anomaly that violates the assumption of a smooth mass distribution and therefore requires substructure (at >99.9% confidence).

6. Application to Observed Lenses

We are now ready to use our theoretical analysis to evaluate the observed lenses, seeking to identify systems that violate the cusp relation and therefore have anomalous flux ratios. We summarize the data in §6.1 and present results in §6.2.

6.1. Data

The data for the seventeen published 4-image lenses are given in Table 1. (The references for all of the lenses are given by Turner et al. 2002.) Only four of the lenses are thought to have cusp configurations, but we can still apply to the cusp relation analysis to all of them to see what we learn. In the table we list the four different image triplets for each lens, with the opening angle θ , the image separation d , and the observed value of R_{cusp} for each. If the lens galaxy position is known, the angle θ is fully determined by the data; if not, we estimate θ using the galaxy position estimated from lens models, which is a fairly model-independent prediction. The separation d is determined directly from the data. To normalize it we need the Einstein radius R_{ein} from lens models, but this again is a model-independent quantity. One can in fact obtain a good estimate of R_{ein} for 4-image lenses merely by drawing a circle through the images, although in practice it may be easier to make simple models. We use isothermal ellipsoid plus shear models, but this choice is not important because all types of models agree on R_{ein} (see Cohn et al. 2001). A technical detail is that we actually normalize d by the model parameter R'_{ein} because this is the most natural approach and it makes our analysis of observed lenses consistent with our Monte Carlo simulations. The difference between R'_{ein} and R_{ein} is unimportant except when the ellipticity is very large (see Figure 11 in Appendix B.2).

The uncertainties in R_{cusp} need to allow for systematic uncertainties in the measured flux ratios due to effects like source variability and the lens time delay, scatter broadening (at radio

wavelengths), and differential extinction by patchy dust in the lens galaxy (at optical wavelengths). (Extinction by dust in our own Galaxy does not affect the flux ratios, because it affects all images equally.) Dalal & Kochanek (2002) advocate adopting a fiducial estimate of 10% uncertainties in the flux ratios to account for these effects, but this is likely to be quite conservative. For the majority of the lenses, we shall see that questions about the size of the uncertainties are irrelevant because the observed values of R_{cusp} are safely within the expected distribution. In Table 1, we therefore simply quote errors for R_{cusp} assuming 10% uncertainties in the individual image flux measurements. However we wish to be more careful in determining a realistic error budget for the four cusp lenses B0712+472, RX J0911+0551, B1422+231, and B2045+265, so we consider them individually in the next section.

Table 1 also gives predicted values for R_{cusp} computed from standard smooth lens models, using the models by Turner et al. (2002). In almost all cases the model consists of an isothermal ellipsoid lens galaxy with an external shear. The only exception is B1555+375, where the ellipsoid plus shear model is somewhat ambiguous and we instead parameterize the angular structure of the lens potential in terms of a shear induced by the matter inside the Einstein ring and an independent shear induced by the matter outside the ring. The models are formally equivalent and differ only in some technical details; see Turner et al. (2002) for more discussion. Also, in MG 0414+0534, RX J0911+0551, and B1608+656 the models include the perturbative effects of an observed satellite galaxy near the main lens galaxy. In general the models reproduce the image positions quite well and only have difficulties reproducing the flux ratios. We stress, though, that the models are not actually used in seeking flux ratio anomalies (other than for estimating R_{ein} , as discussed above). They are included only as a general indication of what to expect for R_{cusp} from smooth lens models for these systems.

6.2. Results

We first use the observed lenses to check the Monte Carlo simulations from §5. If the simulations capture the main features of a realistic lens population, then the *predicted* values of R_{cusp} from models of the known lenses should be consistent with the confidence regions derived from the simulations. Figure 7 shows the model values of R_{cusp} superposed on the predicted confidence contours. A few of the points lie just outside the 99.9% confidence contour (RX J0911+0551 at $\theta = 290^\circ$ in Figure 7a, and B2045+265 and B1422+231 near the “knee” at $d/R_{\text{ein}} \simeq 1.7$ in Figure 7b). However, these correspond to cusp lenses where the models have attempted to reproduce flux ratios that are suspected to be anomalous, adopting some unusual combinations of ellipticity and shear in the process. We do not expect the cusp relation analysis to be useful at large values of θ and d anyway. For the most part, though, we see that the points are indeed consistent with the predicted confidence intervals. We therefore conclude that the Monte Carlo simulations agree well with a realistic lens population.

We are finally ready to evaluate the real data. Figure 8 shows the observed values of R_{cusp} su-

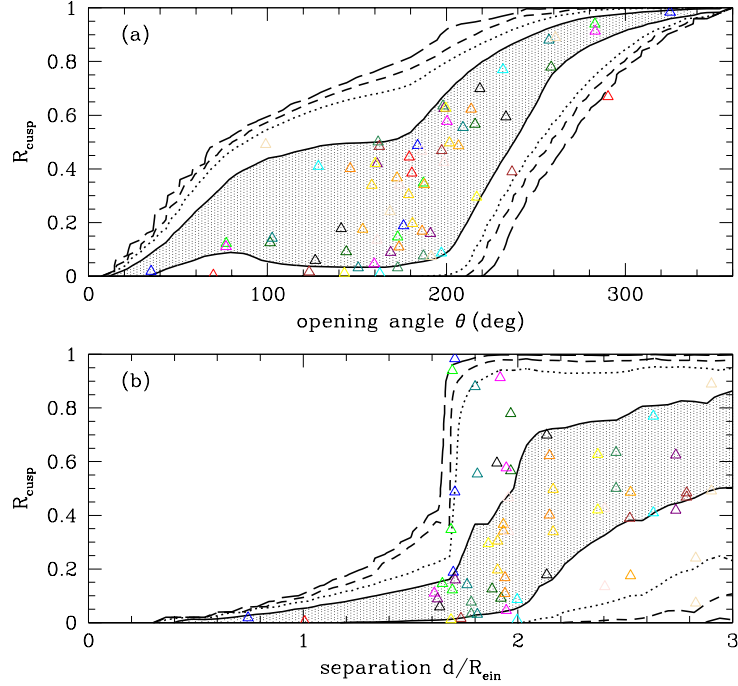


Fig. 7.— The contours are taken from Figure 6. The points show, for comparison, the *predicted* values of R_{cusp} from models of the known 4-image lenses.

perposed on the predicted confidence contours. Most of the observed lenses lie within the predicted confidence region, so according to this analysis they are not obviously inconsistent with smooth lens models. The four cusp lenses can be identified as the four points with $\theta \lesssim 80^\circ$. Two of these lenses are obvious outliers: B2045+265 (Fassnacht et al. 1999) has a triplet with $\theta = 34.9^\circ$, $d/R_{\text{ein}} = 0.74$, and $R_{\text{cusp}} = 0.52$; and RX J0911+0551 (Burud et al. 1998) has a triplet with $\theta = 69.6^\circ$, $d/R_{\text{ein}} = 1.0$, and $R_{\text{cusp}} = 0.22$. Both lenses have clear cusp configurations, as indicated by the small values of θ and d , and they lie above the 99.9% confidence upper limit on R_{cusp} in Figure 8b. Incidentally, B2045+265 is also seen as an outlier in Figure 8a, and is responsible for the possible outlier point at $\theta = 325^\circ$. RX J0911+0551 is responsible for the outlier point at $\theta = 290^\circ$ in Figure 8.

To compare the data and predictions more clearly, Figure 9 shows the predicted conditional probability distributions $p(R_{\text{cusp}}|d)$, $p(R_{\text{cusp}}|\theta)$, and $p(R_{\text{cusp}}|d, \theta)$ for R_{cusp} given values of d and/or θ and/or appropriate for the four cusp lenses (actually, within ± 0.05 in d/R_{ein} and $\pm 5^\circ$ in θ). Although d/R_{ein} and θ separately provide valuable information about the image configuration and the position of the source relative to the cusp, they provide more powerful constraints when taken together. As a practical matter, the joint $p(R_{\text{cusp}}|d, \theta)$ distribution is somewhat noisier than the univariate distributions due to the smaller number of models satisfying the joint constraints, but

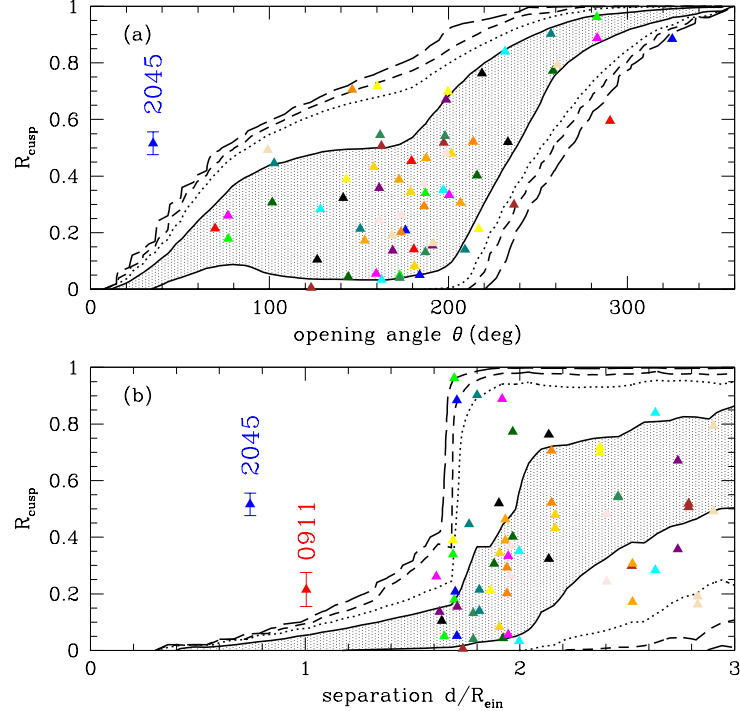


Fig. 8.— Similar to Figure 7, but now the points show the *observed* values of R_{cusp} for the known 4-image lenses. Points from the lenses RX J0911+0551 and B2045+265 are labeled, and have errorbars corresponding to assumed 10% uncertainties in the measured fluxes of the images (see Table 1).

the inferred confidence intervals are still reliable. Figure 9 also shows Gaussians representing the measured values and uncertainties for R_{cusp} in the four cusp lenses. As discussed in §6.1 and below, we consider both a pessimistic case of 10% uncertainties on the image fluxes, and a more realistic case assuming statistical measurement uncertainties. We now discuss each of the four cusp lenses individually.

6.2.1. B2045+265

Fassnacht et al. (1999) give eight measurements of the radio fluxes for B2045+265 at 1.4, 5, 8.5, and 15 GHz, from different radio arrays with different resolutions. The mean value and scatter in R_{cusp} is 0.516 ± 0.018 ; the scatter is only slightly larger than the uncertainty that would be inferred from the quoted flux errors. The fact that the R_{cusp} values from diverse radio datasets are consistent within the errors argues against any significant non-gravitational effects (e.g., scattering). Also, for a cusp triplet the time delays are expected to be very short — predicted to be $\lesssim 6$ hours

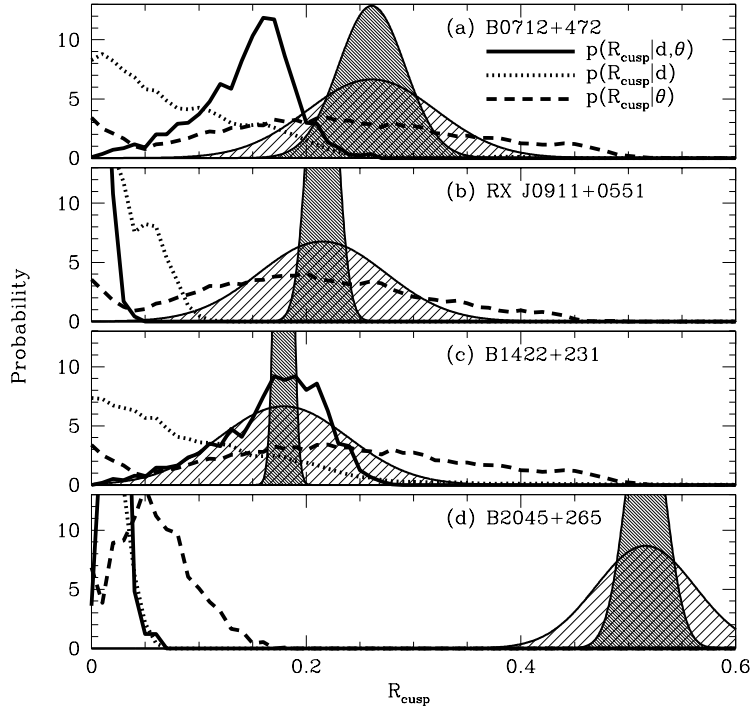


Fig. 9.— The conditional probability distributions $p(R_{\text{cusp}}|d, \theta)$ (solid curves), $p(R_{\text{cusp}}|d)$ (dotted curves), and $p(R_{\text{cusp}}|\theta)$ (dashed curves) for R_{cusp} from the Monte Carlo simulation of a realistic lens population, using the values of θ and d appropriate for each of the four known cusp lenses. The measured values and uncertainties for R_{cusp} are indicated by Gaussians; the light shaded Gaussians correspond to assumed flux uncertainties of 10%, while the heavy shaded Gaussians correspond to more realistic assessments of the statistical flux uncertainties (see text). Each panel shows a different lens system: (a) B0712+472, $d/R_{\text{ein}} = 1.61$, $\theta = 76^\circ.9$. (b) RX J0911+0551, $d/R_{\text{ein}} = 1.00$, $\theta = 69^\circ.6$. (c) B1422+231, $d/R_{\text{ein}} = 1.69$, $\theta = 77^\circ.0$. (d) B2045+265, $d/R_{\text{ein}} = 0.74$, $\theta = 34^\circ.9$.

for B2045+265, and similarly short for the other cusp lenses — so they should have no effect on the measured value of R_{cusp} . We therefore believe that ± 0.018 represents a reasonable estimate of the uncertainty. The uncertainty assuming pessimistic 10% flux errors would be ± 0.046 .

Figures 8 and 9 show that the existence of a flux ratio anomaly in B2045+265 is beyond doubt. Even generous 10% flux uncertainties leave the observed value of R_{cusp} some 10σ above the predicted upper limit. Increasing the ellipticity to an unreasonable value $e \gtrsim 0.9$ helps stretch the $p(R_{\text{cusp}}|\theta)$ distribution toward the observed value of R_{cusp} , but has little effect on the other two distributions. In other words, it is extremely difficult to make any models predict R_{cusp} as large as observed. The robustness of both the observed and predicted results allows us to conclude at very high confidence that B2045+265 has a flux ratio anomaly.

6.2.2. RX J0911+0551

RX J0911+0551 is the only cusp lens where we must rely on optical and near-IR image fluxes and therefore worry about differential extinction. The statistical uncertainties in the fluxes are 2% in the H band and 3–6% in the V and I bands, from Hubble Space Telescope images obtained by CfA/Arizona Space Telescope Lens Survey¹² (Kochanek et al., private communication; also see Burud et al. 1998). Image A₁ has colors $V - H = 1.24$ and $I - H = 0.79$, while images A₂ and A₃ both have colors $V - H = 1.54$ and $I - H = 1.01$. If the color difference is due to dust in the lens galaxy, we estimate that the differential extinction between A₁ and the A₂/A₃ pair is just 0.04 mag in the H band (following the analysis of Falco et al. 1999, using a redshifted $R_V = 3.1$ extinction curve from Cardelli, Clayton & Mathis 1989). Thus, we find $R_{\text{cusp}} = 0.224$ from the raw H-band flux ratios versus $R_{\text{cusp}} = 0.215$ from the extinction-corrected flux ratios. The flux ratios from older deconvolved ground-based images (Burud et al. 1998) give compatible but slightly larger values for R_{cusp} . Propagating the 2% statistical flux uncertainties leads to an uncertainty of ± 0.012 in R_{cusp} . In other words, by working at long wavelengths we can ensure that the effects of differential extinction are smaller than the statistical uncertainties. Combining this argument with the short expected time delays, we believe that ± 0.012 represents a realistic estimate of the uncertainty in R_{cusp} . The uncertainty assuming pessimistic 10% flux errors would be ± 0.059 .

The comparison of the observed and predicted values for R_{cusp} is somewhat more complicated for RX J0911+0551 than it was for B2045+265. The distance of the observed R_{cusp} above the predicted upper limit is such that we must worry about both the uncertainties in the measurements and the assumptions in the Monte Carlo simulations. In particular, the lens galaxy lies in a cluster that contributes a large shear $\gamma \simeq 0.3$ to the lens potential (Kneib, Cohen & Hjorth 2000). This is almost 4σ above the median of our assumed shear distribution, and we saw in Figure 4 of §4 that such large shears can have an important effect on the upper limit on R_{cusp} . To explore this issue, we use another set of Monte Carlo simulations using the same ellipticity distribution as before, but with the shear amplitude fixed at $\gamma = 0.3$; the orientations of the shear and ellipticity axes are still random. Figure 10 shows the resulting conditional probability distributions $p(R_{\text{cusp}}|\theta)$, $p(R_{\text{cusp}}|d)$, and $p(R_{\text{cusp}}|d, \theta)$ for this “cluster shear” case, together with the results for the fiducial shear case.

The large shear increases the tail to large R_{cusp} at fixed d (Figure 10b), causing the predicted distribution to overlap the tail of the Gaussian representing observed value in the case of pessimistic errors. However, the joint distribution $p(R_{\text{cusp}}|d, \theta)$ is considerably more compact, for both the normal and cluster shear cases. To quantify the overlap, we compute the probability in the tail of the distribution, $P(R_{\text{cusp}} > X|d, \theta)$, where X is chosen to correspond to the 3σ lower limit on the observed value of R_{cusp} . Even for pessimistic errors in the observed value ($X = 0.038$), the tail probability is just 0.4% or 0.8% for normal or cluster shear, respectively; for the more realistic observed errors ($X = 0.179$), the tail probability is <0.1%. We can therefore conclude that the

¹²See <http://cfa-www.harvard.edu/castles>.

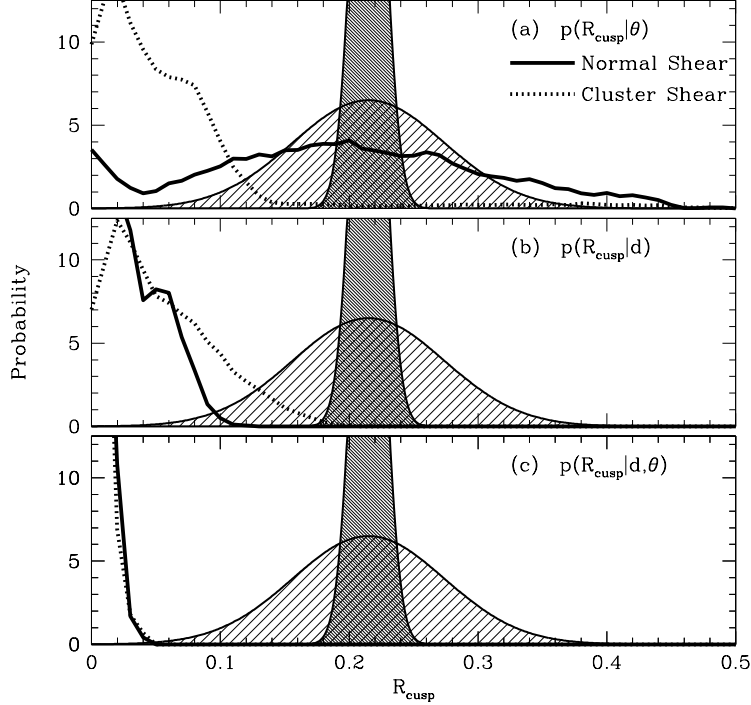


Fig. 10.— In each panel, the heavy solid curve shows the conditional probability distribution of R_{cusp} for Monte Carlo simulations with the fiducial shear distribution, while the dotted curve (“cluster shear”) shows the case with the shear fixed at $\gamma = 0.3$. Also shown are Gaussians representing the measured value and uncertainties for R_{cusp} for RX J0911+0551. (a) The conditional probability distribution $p(R_{\text{cusp}}|\theta)$ for $\theta = 70^\circ \pm 5^\circ$. (b) The conditional probability distribution $p(R_{\text{cusp}}|d)$ for $d/R_{\text{ein}} = 1.00 \pm 0.05$. (c) The joint conditional probability distribution $p(R_{\text{cusp}}|d, \theta)$.

observed value of R_{cusp} is discrepant and that RX J0911+0551 has a flux ratio anomaly at >99% confidence.

6.2.3. B0712+472

Jackson et al. (1998) give three different measurements of the radio fluxes for B0712+472 at 5 GHz and one measurement at 15 GHz, claiming 5-10% uncertainties. The mean and scatter in the value of R_{cusp} from the four datasets is 0.261 ± 0.031 . The uncertainty assuming 10% flux errors would be ± 0.060 .

The evidence for a flux ratio anomaly in B0712+472 is somewhat ambiguous. The cusp image triplet has $d/R_{\text{ein}} = 1.61$ and $\theta = 76^\circ.9$. In Figure 8, we see that the measured value $R_{\text{cusp}} = 0.261$ lies within the 68% contour for $p(R_{\text{cusp}}|\theta)$, but between the 95% and 99% contours for $p(R_{\text{cusp}}|d)$.

In Figure 9 we see that the conditional probability distributions have tails that overlap the observed value of R_{cusp} . To quantify the overlap, we compute the probabilities in the tail of the predicted $p(R_{\text{cusp}}|d, \theta)$ distribution¹³ above some value X , and at the same time the probability in the tail of the observed distribution below X . Using the realistic measurement uncertainties ($R_{\text{cusp}} = 0.261 \pm 0.031$), we find that at $X = 0.209$ both of the tail probabilities are 4.8%. This suggests that the observed value of R_{cusp} is anomalous at the 95% confidence level. (Using pessimistic measurement errors of ± 0.060 , the confidence level would be 88%.) We conclude that the measured value of R_{cusp} for B0712+472 is marginally inconsistent with the cusp relation, but it cannot be identified as anomalous with very high confidence.

6.2.4. B1422+231

Patnaik & Narasimha (2001) report 61 measurements of the radio fluxes for B1422+231 at 8.4 and 15 GHz from a 193-day monitoring campaign. The mean and scatter for R_{cusp} from all of the measurements is 0.179 ± 0.006 . The error on R_{cusp} obtained directly from the individual flux errors is comparable to or smaller than the scatter. The uncertainty assuming 10% flux errors would be ± 0.060 .

It is interesting that this lens is not an outlier in our analysis (see Figures 8 and 9), even though detailed modeling has shown that it has a flux ratio anomaly (Mao & Schneider 1998; Bradač et al. 2002; Metcalf & Zhao 2002; Keeton 2002b). The reason is that we are focusing on the *maximum allowed* values of R_{cusp} as a function of θ and d . We are not considering whether the models that can produce those values are at all consistent with the observed image positions. In other words, we are throwing away reliable information in our attempt to be as general and robust as possible. Metcalf & Zhao (2002) demonstrate that imposing the position constraints via detailed lens modeling provides a more sophisticated analysis that has more power to identify flux ratio anomalies. But because it relies on specific modeling, we believe that model fitting is less robust than the cusp relation analysis. Furthermore, such fitting is difficult to interpret; it is not immediately clear from the results of such an analysis exactly why the model fails. Our goal with the cusp relation analysis has been to develop a method for identifying flux ratio anomalies that is robust, conservative, and easy to interpret.

6.2.5. Comments

To conclude this section, we remark that it is surprising to see how large R_{cusp} can be for realistic lenses, *even in the absence of substructure*. Image triplets must be quite tight in order to satisfy the cusp magnification relation well. To satisfy the relation to better than 10% (at

¹³Although it may not be obvious from Figure 9, the $p(R_{\text{cusp}}|d, \theta)$ distribution actually has the smallest tail.

99% confidence), the opening angle must be $\theta \lesssim 30^\circ$ or $d/R_{\text{ein}} \lesssim 1$ (also see Appendix C). The available parameter space that gives rise to such image configurations is generally expected to be quite small; for example, from the Monte Carlo simulations we expect $\sim 0.1\%$ of 4-image lenses to have cusp triplets that satisfy both of these conditions. While this estimate does not take into account magnification bias, which will work in favor of tight configurations, it does suggest that cusp image configurations that are close to ideal (in the sense of satisfying the cusp relation) are likely to be rare. The cusp relation can still be a powerful tool for identifying flux ratio anomalies, but it must be used with some care.

7. Conclusions

There exist universal relations between the positions and magnifications of images associated with ideal cusp and fold catastrophes. For cusps, the main relation of interest says that the signed magnifications of the three images should sum to zero. (There are two more independent magnification relations, but they involve unobservable quantities.) The relations can be violated only if: (1) the lens model is smooth but the true caustic is not well approximated as an *ideal* cusp or fold; or (2) there are density fluctuations in the lensing potential on scales smaller than the separations between the images. We have studied case 1 and quantified how the ideal magnification relation can be violated for realistic (non-ideal) cusps. Any violation of the realistic cusp magnification relation therefore implies case 2: there must be small-scale structure in the lens galaxy.

The realistic cusp relation is expressed in terms of upper limits on $R_{\text{cusp}} = (F_1 + F_2 + F_3) / (|F_1| + |F_2| + |F_3|)$ where the F_i are the signed fluxes for a triplet of images. The upper limits depend mainly on the ellipticity of the lens galaxy and the shear from the environment, and are not very sensitive to the radial profile of the lens galaxy. We have derived analytic expressions for the upper limit on R_{cusp} for given values of the ellipticity and shear. In general, the upper limit scales as $R_{\text{cusp}} \propto \theta^2 \propto d^2$ for small values of the opening angle θ and image separation d of the image triplet. We have also derived confidence limits on R_{cusp} for a distribution of ellipticities and shears describing a realistic population of lens galaxies.

Of the four cusp lenses in our sample, two clearly violate the cusp relation (B2045+265 and RX J0911+0551). Because of the generality of the cusp relation analysis, we can say with high confidence that no (reasonable) smooth lens model can reproduce the observed flux ratios in these two lenses. This conclusion formally depends on assumptions about the distribution of ellipticity and shear in a realistic lens population, but in practice the ellipticity would have to be unacceptably large in order to reproduce the observed large values of R_{cusp} . So we can say with high confidence that RX J0911+0551 and B2045+265 require small-scale structure in the lens galaxy. The lens B0712+472 has a measured value of R_{cusp} that is marginally anomalous at the 95% confidence level.

The lens B1422+231 does not violate the basic cusp relation, even though it is known from

detailed modeling to have a flux ratio anomaly (Mao & Schneider 1998; Bradač et al. 2002; Metcalf & Zhao 2002; Keeton 2002b). This is because in our analysis of the cusp relation we have ignored constraints from the observed image positions, in order to be general and to avoid modeling as much as possible. The idea is that an analysis based purely on magnification relations is the most robust and conservative way to identify flux ratio anomalies. Adding constraints from the image positions yields an analysis that is more sophisticated and has more power to identify flux ratio anomalies (see Metcalf & Zhao 2002 for a good example), but it requires detailed modeling and is therefore less robust. The cusp relation also reveals, more clearly than modeling can, just why the flux ratios are difficult to fit. In our opinion, the cusp relation analysis is the best place to start when seeking to identify lenses with flux ratio anomalies (at least for lenses in cusp configurations). If an observed lens violates the cusp relation then the anomaly is unambiguous and easy to understand. If it does not violate the cusp relation, it may still have an anomaly but may only be revealed by more sophisticated and less model-independent analyses.

Our cusp relation analysis has revealed only two lenses with unambiguous flux ratio anomalies, plus one other candidate; but perhaps that is not surprising, because only four of the 17 known 4-image lenses have cusp configurations. Another seven lenses have fold configurations, for which there is an analogous fold magnification relation. Studying the fold relation and applying it to observed lenses is the subject of a forthcoming paper (Gaudi et al., in preparation).

Throughout this paper we have not spoken about the cause of flux ratio anomalies, other than to describe it as structure in the lens galaxy on scales smaller than the separations between the images. The two main classes of substructure discussed in the literature are stars in the lens galaxy (e.g., Chang & Refsdal 1979; Paczyński 1986; Irwin et al. 1989; Witt, Mao & Schechter 1995; Schechter & Wambsganss 2002) and galactic subhalos with characteristic mass 10^4 – $10^8 M_\odot$ left over from hierarchical structure formation (Mao & Schneider 1998; Metcalf & Madau 2001; Chiba 2002; Dalal & Kochanek 2002). It is likely that both are at work in the known lenses. Other types of small-scale structure may be at work as well. It will be important to distinguish all the different cases, because they have very different astrophysical applications and implications. Nevertheless, the essential first step in any study of substructure lensing is simply to identify anomalous flux ratios. The cusp relation analysis will therefore be valuable for any application that relies on finding lenses that cannot be fit with smooth lens models.

We would like to thank the organizers of the 2002 Ringberg Workshop on Gravitational Lenses, where this work was conceived, and Paul Schechter for his list of 13 Provocations; this work addresses Provocation #9. We also thank Neal Dalal, Gil Holder, and Rennan Barkana for interesting discussions. We thank Christina Turner for providing model results in advance of publication. This work was supported by NASA through Hubble Fellowship grants from the Space Telescope Science Institute, which is operated by the Association of Universities for Research in Astronomy, Inc., under NASA contract NAS5-26555; by JPL contract 1226901; by an Alfred P. Sloan Research Fellowship; and by NSF Career grant DMS-98-96274.

A. Universal Relations for Cusps

In this Appendix we study the general properties of the lensing map near a cusp catastrophe to derive generic relations between the image positions and magnifications that should be satisfied for any (smooth) lens model when the source is sufficiently close to a cusp.

A.1. Local orthogonal coordinates

Consider the lens equation

$$\mathbf{y} = \mathbf{x} - \text{grad } \psi(\mathbf{x}). \quad (\text{A1})$$

Assume that the induced lensing map, $\boldsymbol{\eta}(\mathbf{x}) = \mathbf{x} - \text{grad } \psi(\mathbf{x})$, from the lens plane L to the light source plane S is locally stable, which yields that the caustics of $\boldsymbol{\eta}$ are either folds or cusps (Petters et al. 2001, p. 294). Then translate coordinates in the lens and light source planes so that the cusp point of interest is at the origin and the critical point mapping to the cusp is also at the origin, i.e., $\boldsymbol{\eta}(\mathbf{0}) = \mathbf{0}$. By abuse of notation, the resulting translations of \mathbf{x} and \mathbf{y} will still be denoted by those symbols.

We now define a change of coordinates about the origins of the lens and light source planes: $\mathbf{x} \rightarrow \boldsymbol{\theta}$, $\mathbf{y} \rightarrow \mathbf{u}$. The coefficients of the quadratic terms of the Taylor expansion of ψ at the origin are

$$\hat{a} = \frac{1}{2}\psi_{11}(\mathbf{0}), \quad \hat{b} = \psi_{12}(\mathbf{0}), \quad \hat{c} = \frac{1}{2}\psi_{22}(\mathbf{0}), \quad (\text{A2})$$

where the subscripts indicate partial derivatives relative to $\mathbf{x} = (x_1, x_2)$. Since the origin is a cusp critical point, $(1 - 2\hat{a})$ and $(1 - 2\hat{c})$ cannot both vanish (Petters et al. 2001, p. 349). Without loss of generality, we shall assume that $(1 - 2\hat{a}) \neq 0$. Define an orthogonal matrix as follows:

$$\mathbf{M} = \frac{1}{\sqrt{(1 - 2\hat{a})^2 + \hat{b}^2}} \begin{bmatrix} 1 - 2\hat{a} & -\hat{b} \\ \hat{b} & 1 - 2\hat{a} \end{bmatrix}. \quad (\text{A3})$$

The new coordinate systems are defined by

$$\boldsymbol{\theta} = (\theta_1, \theta_2) \equiv \mathbf{M} \mathbf{x}, \quad \mathbf{u} = (u_1, u_2) \equiv \mathbf{M} \mathbf{y}. \quad (\text{A4})$$

Note that this is the *same* coordinate change in the lens and light source planes, and the coordinates depend on the potential.

It can be proven rigorously that the lensing map $\boldsymbol{\eta}$ in the orthogonal coordinates (A4) can be approximated in a neighborhood of the cusp critical point at the origin by a simple polynomial mapping (Petters et al. 2001, pp. 341-353; also see Schneider et al. 1992, p. 193):

$$u_1 = c \theta_1 + \frac{b}{2} \theta_2^2, \quad u_2 = b \theta_1 \theta_2 + a \theta_2^3, \quad (\text{A5})$$

where

$$\begin{aligned} a &= -\frac{1}{6}\psi_{2222}(\mathbf{0}), & b &= -\psi_{122}(\mathbf{0}) \neq 0, \\ c &= 1 - \psi_{11}(\mathbf{0}) \neq 0, & 2ac - b^2 &\neq 0. \end{aligned} \quad (\text{A6})$$

The partial derivatives of ψ are relative to the original coordinates $\mathbf{x} = (x_1, x_2)$. The origin in the light source plane is called a *positive cusp* if $2ac > b^2$ and a *negative cusp* if $2ac < b^2$. A source inside a positive cusp has, locally, two images with positive parity and one with negative parity; the reverse is true for negative cusps.

A.2. Position relations

Using the lens equation (A5), the three local lensed images associated with a source inside and close to the cusp have the following positions (e.g., Gaudi & Petters 2002):

$$\boldsymbol{\theta}_i = \left(\frac{u_1}{c} - \frac{b}{2c} z_i^2, z_i \right), \quad i = 1, 2, 3. \quad (\text{A7})$$

The z_i are the three real solutions of the cubic equation

$$z^3 + p z + q = 0, \quad (\text{A8})$$

where

$$p = \frac{2b}{2ac - b^2} u_1 \equiv \hat{p} u_1, \quad q = -\frac{2c}{2ac - b^2} u_2 \equiv -\hat{q} u_2. \quad (\text{A9})$$

Note that when the source is inside the cusp the discriminant,

$$D = \left(\frac{p}{3} \right)^3 + \left(\frac{q}{2} \right)^2 = \frac{4(\hat{p} u_1)^3 + 27(\hat{q} u_2)^2}{108}, \quad (\text{A10})$$

is negative so eq. (A8) does have three real roots.

The usual factoring of a cubic polynomial yields:

$$0 = (z - z_1)(z - z_2)(z - z_3), \quad (\text{A11})$$

$$= z^3 - [z_1 + z_2 + z_3]z^2 + [z_1 z_2 + z_1 z_3 + z_2 z_3]z - [z_1 z_2 z_3]. \quad (\text{A12})$$

Identifying coefficients with eq. (A8) yields three relations between the image positions:

$$z_1 + z_2 + z_3 = 0, \quad (\text{A13})$$

$$z_1 z_2 + z_1 z_3 + z_2 z_3 = \hat{p} u_1, \quad (\text{A14})$$

$$z_1 z_2 z_3 = \hat{q} u_2. \quad (\text{A15})$$

These are universal relations satisfied by the image positions of a triplet associated with a source near a cusp. Two additional relations can be obtained respectively by squaring (A13) and using (A14), and squaring (A14) and using (A13):

$$z_1^2 + z_2^2 + z_3^2 = -2\hat{p}u_1, \quad (A16)$$

$$(z_1z_2)^2 + (z_1z_3)^2 + (z_2z_3)^2 = (\hat{p}u_1)^2. \quad (A17)$$

These relations are not independent of (A13)–(A15), but they are more useful in certain circumstances (as seen below).

A.3. Magnification relations

The signed magnification of each image θ_i in the triplet associated with the cusp is given by

$$\mu_i = \frac{1}{\det[\text{Jac } \mathbf{u}](\theta_i)} = \frac{\hat{p}}{b(\hat{p}u_1 + 3z_i^2)}, \quad i = 1, 2, 3, \quad (A18)$$

where $\text{Jac } \mathbf{u}$ is the Jacobian matrix of the lensing map (A5). Note that $\text{Jac } \mathbf{u} = M \text{Jac } \mathbf{y}$, so with M an orthogonal matrix we verify that the magnification is independent of our choice of coordinates: $\det[\text{Jac } \mathbf{u}] = \det[\text{Jac } \mathbf{y}]$.

Three known universal relations between the magnifications μ_i are as follows (Schneider & Weiss 1992; Zakharov 1995; Petters et al. 2001, p. 339):

$$\mu_1 + \mu_2 + \mu_3 = 0, \quad (A19)$$

$$\mu_1\mu_2 + \mu_1\mu_3 + \mu_2\mu_3 = -\frac{\hat{p}^3 u_1}{36 b^2 D}, \quad (A20)$$

$$\mu_1\mu_2\mu_3 = \frac{\hat{p}^3}{108 b^3 D}. \quad (A21)$$

where D is given by eq. (A10). These relations can be verified by direct calculation from (A18), using the position relations (A15)–(A17) for simplifications. In analogy with the position relations, we can derive additional magnification relations:

$$\mu_1^2 + \mu_2^2 + \mu_3^2 = \frac{\hat{p}^3 u_1}{18 b^2 D}, \quad (A22)$$

$$(\mu_1\mu_2)^2 + (\mu_1\mu_3)^2 + (\mu_2\mu_3)^2 = \left(\frac{\hat{p}^3 u_1}{36 b^2 D}\right)^2. \quad (A23)$$

These quadratic magnification sum rules have not appeared in the literature before.

B. Simple Lens Models

In this Appendix we derive exact solutions to the lens equation to use as a benchmark for understanding the cusp relations. Exact solutions are possible only for certain lens models, and

then only for sources on a symmetry axis. We consider two families of models: a spherical galaxy with a power law density profile and an external shear; and a singular isothermal ellipsoid with an external shear aligned with the major or minor axis of the ellipse.

B.1. Power law galaxy plus shear

Consider the lensing potential

$$\psi(r, \phi) = \frac{1}{\alpha} R_{\text{ein}}^{2-\alpha} r^\alpha - \frac{\gamma}{2} r^2 \cos 2\phi. \quad (\text{B1})$$

The second term represents an external shear with amplitude γ ; shears with $\gamma > 0$ or $\gamma < 0$ are aligned with the horizontal or vertical axis, respectively. The first term in the potential represents a spherical galaxy with a power law profile for the surface mass density,

$$\kappa(r) = \frac{\Sigma(r)}{\Sigma_{\text{crit}}} = \frac{\alpha}{2} \left(\frac{R_{\text{ein}}}{r} \right)^{2-\alpha}, \quad (\text{B2})$$

where R_{ein} is the Einstein radius. The case $\alpha = 1$ corresponds to a singular isothermal sphere (SIS), while the cases $\alpha < 1$ and $\alpha > 1$ correspond respectively to steeper and shallower profiles, respectively.

The lens equation has the form

$$y_1 = r \cos \phi \left[1 + \gamma - \left(\frac{R_{\text{ein}}}{r} \right)^{2-\alpha} \right], \quad (\text{B3})$$

$$y_2 = r \sin \phi \left[1 - \gamma - \left(\frac{R_{\text{ein}}}{r} \right)^{2-\alpha} \right], \quad (\text{B4})$$

and the lensing magnification μ is given by

$$\mu^{-1} = 1 - \gamma^2 - (1 - \alpha) \left(\frac{R_{\text{ein}}}{r} \right)^{4-2\alpha} - \left(\frac{R_{\text{ein}}}{r} \right)^{2-\alpha} [\alpha + (2 - \alpha)\gamma \cos 2\phi]. \quad (\text{B5})$$

The critical curve in the image plane is the curve where $\mu^{-1} = 0$, and it maps to the caustic curve in the source plane. The caustic has a cusp on the horizontal axis at position $(y_{1c}, 0)$, which corresponds to a point on the critical curve at position $(x_{1c}, 0)$, where

$$x_{1c} = \frac{R_{\text{ein}}}{(1 - \gamma)^{1/(2-\alpha)}}, \quad (\text{B6})$$

$$y_{1c} = \frac{2\gamma R_{\text{ein}}}{(1 - \gamma)^{1/(2-\alpha)}}. \quad (\text{B7})$$

The Taylor series coefficients used to define the local orthogonal coordinate system in Appendix A.1 are as follows:

$$\hat{a} = \frac{1}{2} [-1 + \alpha(1 - \gamma)] , \quad \hat{b} = 0 , \quad \hat{c} = \frac{1}{2} , \quad (B8)$$

$$a = \frac{2 - \alpha}{2R_{\text{ein}}^2} (1 - \gamma)^{(4-\alpha)/(2-\alpha)} , \quad c = 2 - \alpha(1 - \gamma) , \quad (B9)$$

$$b = \frac{2 - \alpha}{R_{\text{ein}}} (1 - \gamma)^{(3-\alpha)/(2-\alpha)} , \quad \hat{p} = \frac{R_{\text{ein}}}{\gamma(1 - \gamma)^{1/(2-\alpha)}} . \quad (B10)$$

Hence the transformation matrix M in eq. (A4) is the identity matrix, so the θ and u coordinate systems are simply the x and y coordinate systems translated so the cusp point is at the origin.

Note that although the potential ψ is not well defined in the limit $\alpha \rightarrow 0$, the lens equation and magnification and other quantities are perfectly well defined and correspond to a point mass in a shear field. Furthermore, in this limit the surface mass density Σ is a δ -function as expected for a point mass. Hence in this formalism we can consider the case $\alpha = 0$ to correspond to a point mass lens.

Consider a source on the horizontal axis inside the astroid caustic; for $\gamma > 0$ ($\gamma < 0$) this correspond to the major (minor) axis of the lens potential. The lens equation can be solved exactly because of symmetry. There is at least one image on the x_1 -axis,¹⁴ and two images off the x_1 -axis. By symmetry, the two off-axis images are identical modulo some signs. To find the positions of these two images, note that with $y_2 = 0$ and $\phi \neq 0$ the only way for eq. (B4) to be satisfied is for the term in square brackets to vanish. This condition yields the polar radius, which can then be substituted into eq. (B3) to find the polar angle. Thus, the positions of the two off-axis images, which we label A and C, are

$$r_A = r_C = \frac{R_{\text{ein}}}{(1 - \gamma)^{1/(2-\alpha)}} , \quad (B11)$$

$$\phi_A = -\phi_C = \cos^{-1} \left(\frac{y_1}{y_{1c}} \right) , \quad (B12)$$

where y_{1c} is given by eq. (B7). Their magnifications of these two images are

$$\mu_A = \mu_C = \left\{ 2\gamma(1 - \gamma)(2 - \alpha) \left[1 - \left(\frac{y_1}{y_{1c}} \right)^2 \right] \right\}^{-1} . \quad (B13)$$

For the on-axis image, which we label B, eq. (B4) is satisfied trivially ($y_2 = 0$ and $\phi_B = 0$). Eq. (B3) can be solved analytically for integer and half-integer values of α , yielding:

$$\alpha = 0 : \quad r_B = \frac{y_1 + \sqrt{y_1^2 + 4(1 + \gamma)R_{\text{ein}}^2}}{2(1 + \gamma)} \quad (B14)$$

¹⁴A “naked” cusp has only one image on the x_1 -axis, while a “clothed” cusp has two. We are interested in only one of the images, so we do not further distinguish between naked and clothed cusps in the analytic work.

$$\alpha = \frac{1}{2} : \quad r_B = \frac{(\xi + y_1)^2}{3\xi(1 + \gamma)} \quad (\text{see below}) \quad (\text{B15})$$

$$\alpha = 1 : \quad r_B = \frac{y_1 + R_{\text{ein}}}{1 + \gamma} \quad (\text{B16})$$

$$\alpha = \frac{3}{2} : \quad r_B = \frac{R_{\text{ein}} + 2(1 + \gamma)y_1 + \sqrt{R_{\text{ein}}[R_{\text{ein}} + 4(1 + \gamma)y_1]}}{2(1 + \gamma)^2} \quad (\text{B17})$$

In the result for $\alpha = 1/2$, ξ is given by

$$\xi^3 = \frac{27}{2}(1 + \gamma)R_{\text{ein}}^3 - y_1^3 + \frac{3}{2} \{ 3(1 + \gamma)R_{\text{ein}}^3 [27(1 + \gamma)R_{\text{ein}}^3 - 4y_1^3] \}^{1/2}. \quad (\text{B18})$$

The magnification μ_B of image B can then be computed from eq. (B5).

B.2. Isothermal ellipsoid plus aligned shear

Now consider a singular isothermal ellipsoid mass distribution, where the surface mass density in units of the critical density is

$$\kappa(r, \phi) = \frac{\Sigma(r, \phi)}{\Sigma_{\text{crit}}} = \frac{R'_{\text{ein}}}{2r\sqrt{1 - \varepsilon \cos 2\phi}}, \quad (\text{B19})$$

Without loss of generality we are working in coordinates that are either aligned with or perpendicular to the major axis of the ellipse. The parameter ε is related to the axis ratio q of the ellipse by $\varepsilon = (1 - q^2)/(1 + q^2)$, so it is not the true ellipticity $e = 1 - q$ but it is a more convenient parameter in this formalism. The scale length R'_{ein} is equal to the Einstein radius when the galaxy is circular, but it is slightly different when the galaxy is elongated. One way to estimate the difference is to consider the monopole deflection of the galaxy (see Cohn et al. 2001), which implies an Einstein radius

$$R_{\text{ein}} = R'_{\text{ein}} \frac{2}{\pi\sqrt{1 - \varepsilon}} K\left(-\frac{2\varepsilon}{1 - \varepsilon}\right), \quad (\text{B20})$$

where $K(x)$ is the complete elliptic integral of the first kind. Figure 11 shows that the difference between R'_{ein} and R_{ein} is only a few percent for moderately elongated galaxies, and becomes noticeable only as the galaxy becomes highly flattened.

We also consider an external shear γ that is *aligned with the major or minor axis of the ellipse*. We cannot consider shears with arbitrary orientations as this would spoil the symmetry that makes it possible to solve the lens equation analytically. Nevertheless, these two cases should bound the interesting range. A single formalism can be used for both cases, where $\gamma > 0$ represents a shear along the major axis and $\gamma < 0$ a shear along the minor axis.

In the following expressions, we assume that the source is on the horizontal (y_1) axis. With appropriate choices of signs for ε and γ we can describe the behavior of a source on either the major or minor axis of the lens potential in all possible combinations of ellipticity and aligned or

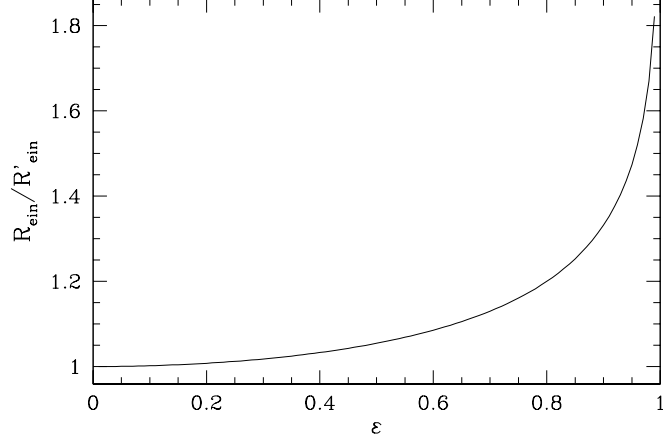


Fig. 11.— Ratio of the estimated Einstein radius R_{ein} to the parameter R'_{ein} as a function of ε .

anti-aligned shear. When ε and γ have the same sign the shear is aligned; the case $\varepsilon > 0$ and $\gamma > 0$ describes a source on the major axis, while the case $\varepsilon < 0$ and $\gamma < 0$ describes a source on the minor axis. When ε and γ have opposite signs the shear is anti-aligned, and the situation is more complicated because the caustic can develop swallowtail catastrophes (Keeton et al. 2000). Briefly, if ellipticity dominates the potential then the case $\varepsilon > 0$ and $\gamma < 0$ describes a major axis cusp while $\varepsilon < 0$ and $\gamma > 0$ describes a minor axis cusp; and vice versa if shear dominates the potential. This formalism breaks down when the caustic has swallowtails (because the nature of the cusp changes). For minor axis cusps the breakdown occurs when ε and γ have opposite signs and

$$\frac{|\varepsilon|}{3 + 2|\varepsilon|} < |\gamma| < \frac{|\varepsilon|}{3 - 2|\varepsilon|} , \quad (\text{B21})$$

while for major axis cusps there is a similar but more complicated expression. See Keeton et al. (2000) for details.

The lens equation has the form (Kassiola & Kovner 1993; Kormann, Schneider & Bartelmann 1994; Keeton & Kochanek 1998)

$$y_1 = (1 + \gamma) r \cos \phi - \frac{R'_{\text{ein}}}{\sqrt{2\varepsilon}} \tan^{-1} \left[\frac{\sqrt{2\varepsilon} \cos \phi}{\sqrt{1 - \varepsilon \cos 2\phi}} \right] , \quad (\text{B22})$$

$$y_2 = (1 - \gamma) r \sin \phi - \frac{R'_{\text{ein}}}{\sqrt{2\varepsilon}} \tanh^{-1} \left[\frac{\sqrt{2\varepsilon} \sin \phi}{\sqrt{1 - \varepsilon \cos 2\phi}} \right] , \quad (\text{B23})$$

and the lensing magnification is μ given by

$$\mu^{-1} = 1 - \gamma^2 - \frac{R'_{\text{ein}}}{r} \frac{1 + \gamma \cos 2\phi}{\sqrt{1 - \varepsilon \cos 2\phi}} . \quad (\text{B24})$$

The critical curve in the image plane is the curve where $\mu^{-1} = 0$, which maps to the caustic in the source plane. The caustic has a cusp at position $(y_{1c}, 0)$, which corresponds to a point on the

critical curve at position $(x_{1c}, 0)$, where

$$x_{1c} = \frac{R'_{\text{ein}}}{(1-\gamma)\sqrt{1-\varepsilon}} , \quad (\text{B25})$$

$$y_{1c} = R'_{\text{ein}} \left[\frac{1+\gamma}{(1-\gamma)\sqrt{1-\varepsilon}} - \frac{1}{\sqrt{2\varepsilon}} \tan^{-1} \sqrt{\frac{2\varepsilon}{1-\varepsilon}} \right] . \quad (\text{B26})$$

The Taylor series coefficients used to define the local orthogonal coordinate system in Appendix A.1 are as follows:

$$\hat{a} = -\frac{\gamma}{2} , \quad \hat{b} = 0 , \quad \hat{c} = \frac{1}{2} , \quad (\text{B27})$$

$$a = \frac{(3-\varepsilon)(1-\gamma)^3}{6(R'_{\text{ein}})^2} , \quad c = 1+\gamma , \quad (\text{B28})$$

$$b = \frac{\sqrt{1-\varepsilon}(1-\gamma)^2}{R'_{\text{ein}}} , \quad \hat{p} = \frac{3\sqrt{1-\varepsilon}R'_{\text{ein}}}{(1-\gamma)(\varepsilon+3\gamma-2\varepsilon\gamma)} . \quad (\text{B29})$$

Hence the transformation matrix \mathbf{M} in eq. (A4) is the identity matrix, so the $\boldsymbol{\theta}$ and \mathbf{u} coordinate systems are simply the \mathbf{x} and \mathbf{y} coordinate systems translated so the cusp point is at the origin.

A source on the horizontal axis inside the astroid caustic has at least one image on the x_1 -axis and two images off the x_1 -axis. Because of the transcendental functions, it is easier to take the polar angle ϕ of an off-axis image as the independent parameter, rather than the source position y_1 . Note that ϕ is related to the opening angle θ defined in §2 by $\theta = 2\phi$. Because of symmetry the two off-axis images are identical modulo some signs. The polar radius for these two images, labeled A and C, is found by requiring that eq. (B23) have a non-trivial solution (i.e., $\phi \neq 0$):

$$r_A = r_C = \frac{R'_{\text{ein}}}{\sqrt{2\varepsilon}(1-\gamma)\sin\phi} \tanh^{-1} \left[\frac{\sqrt{2\varepsilon} \sin\phi}{\sqrt{1-\varepsilon}\cos 2\phi} \right] , \quad (\text{B30})$$

$$\phi_A = -\phi_C \equiv \phi \quad (\text{B31})$$

The corresponding source position is, from eq. (B22),

$$y_1 = \frac{(1+\gamma)\cos\phi}{(1-\gamma)\sin\phi} \frac{R'_{\text{ein}}}{\sqrt{2\varepsilon}} \tanh^{-1} \left[\frac{\sqrt{2\varepsilon} \sin\phi}{\sqrt{1-\varepsilon}\cos 2\phi} \right] - \frac{R'_{\text{ein}}}{\sqrt{2\varepsilon}} \tan^{-1} \left[\frac{\sqrt{2\varepsilon} \cos\phi}{\sqrt{1-\varepsilon}\cos 2\phi} \right] . \quad (\text{B32})$$

Finally, the position of the on-axis image (labeled B) is found by solving eq. (B22) with $\phi_B = 0$:

$$r_B = \frac{1}{1+\gamma} \left[y_1 + \frac{R'_{\text{ein}}}{\sqrt{2\varepsilon}} \tan^{-1} \sqrt{\frac{2\varepsilon}{1-\varepsilon}} \right] . \quad (\text{B33})$$

The magnifications of all three image can be computed from these positions using eq. (B24).

C. Cusp position relations in simple models

In this Appendix we check the cusp position relations using the analytic solutions for simple lens models. For simplicity, here we work in units with $R_{\text{ein}} = 1$. Consider sources lying on the cusp symmetry axis. Note that an image with polar coordinates (r_i, ϕ_i) in Appendix B corresponds to $z_i = r_i \sin \phi_i$ in the coordinate system used in Appendix A. By symmetry, a source on the axis always has two images off the axis and one image on the axis such that $z_1 > 0$, $z_2 = 0$, and $z_3 = -z_1 < 0$. Therefore the two position relations (A13) and (A15) are satisfied *by symmetry*. All that remains is to check the symmetric sum rule eq. (A14).

For the power law galaxy plus shear models of Appendix B.1, the exact solution of the lens equation yields the left-hand side of the position sum rule,

$$z_1 z_2 + z_1 z_3 + z_2 z_3 = \frac{u_1}{\gamma(1-\gamma)^{1/(2-\alpha)}} + \frac{u_1^2}{4\gamma^2} . \quad (\text{C1})$$

At the same time, combining the Taylor coefficients for this model into the right-hand side of the sum rule yields

$$\hat{p} u_1 = \frac{u_1}{\gamma(1-\gamma)^{1/(2-\alpha)}} . \quad (\text{C2})$$

The left and right-hand sides agree to first order in u_1 , the distance of the source from the cusp. However, they disagree at second order, with an error

$$E_{\text{pos}} = \frac{u_1^2}{4\gamma^2} = \frac{4 \sin^4(\theta/4)}{(1-\gamma)^{2/(2-\alpha)}} , \quad (\text{C3})$$

where θ is the opening angle of the image triplet, as defined in §2. This result holds for all values of α . We see that the ideal position relation is satisfied for sources asymptotically close to the cusp but violated for sources farther away, with a scaling $E_{\text{pos}} \propto u_1^2 \propto \theta^4$. This error arises directly from the breakdown of the polynomial map eq. (A5) as a good approximation of the true lensing map.

For real lenses the left-hand side of the position sum rule will have some measurement uncertainty. If the position uncertainty is σ_x , the inferred uncertainty in the left-hand side of the position relation will be $E_{\text{meas}} \simeq \sigma_x \sin(\theta/2)$. Typical position uncertainties from Hubble Space Telescope observations of 4-image lenses are ~ 3 mas, or $\sigma_x \sim 0.002$ in units with $R_{\text{ein}} = 1$. In this case the opening angle must be $\theta \lesssim 20^\circ$ in order for the analytic errors to be smaller than the measurement uncertainties, using eq. (C3) with reasonable values of α and γ . In other words, only image triplets that are relatively tight correspond to sources close enough to the cusp that the analytic errors are smaller than measurement uncertainties.

Table 1. Observed 4-Image Lenses

| Lens | Type | R_{ein} (") | Triplet | θ (°) | d (") | Data | R_{cusp} Model |
|----------------|-------------------|----------------------|--|--------------|---------|-----------|----------------------------|
| B0128+437 | radio, fold | 0.20 | BCD | 236.7 | 0.50 | 0.30±0.06 | 0.39 |
| | | | ACD | 197.4 | 0.55 | 0.52±0.05 | 0.47 |
| | | | ABD | 123.3 | 0.34 | 0.01±0.06 | 0.02 |
| | | | ABC | 162.6 | 0.55 | 0.51±0.05 | 0.48 |
| HE 0230–2130 | optical, fold | 0.83 | A ₂ BC | 197.2 | 1.66 | 0.35±0.06 | 0.09 |
| | | | A ₁ BC | 231.6 | 2.19 | 0.84±0.02 | 0.77 |
| | | | A ₁ A ₂ C | 162.8 | 1.66 | 0.03±0.07 | 0.01 |
| | | | A ₁ A ₂ B | 128.4 | 2.19 | 0.28±0.06 | 0.41 |
| MG 0414+0534 | near-IR, fold | 1.08 | A ₂ BC | 216.0 | 2.13 | 0.40±0.05 | 0.57 |
| | | | A ₁ BC | 258.5 | 2.13 | 0.77±0.03 | 0.78 |
| | | | A ₁ A ₂ C | 144.0 | 2.08 | 0.04±0.06 | 0.09 |
| | | | A ₁ A ₂ B | 101.5 | 2.03 | 0.31±0.06 | 0.13 |
| HE 0435–1223 | optical, cross | 1.18 | BCD | 179.0 | 2.25 | 0.34±0.05 | 0.30 |
| | | | ACD | 201.7 | 2.56 | 0.48±0.05 | 0.50 |
| | | | ABD | 181.0 | 2.25 | 0.08±0.06 | 0.20 |
| | | | ABC | 158.3 | 2.56 | 0.43±0.05 | 0.34 |
| B0712+472 | radio, cusp | 0.65 | BCD | 200.4 | 1.27 | 0.33±0.06 | 0.58 |
| | | | ACD | 283.1 | 1.25 | 0.89±0.01 | 0.91 |
| | | | ABD | 159.6 | 1.27 | 0.06±0.07 | 0.05 |
| | | | ABC* | 76.9 | 1.05 | 0.26±0.06 | 0.11 |
| RX J0911+0551 | near-IR, cusp | 0.96 | A ₂ A ₃ B | 179.4 | 3.26 | 0.45±0.05 | 0.45 |
| | | | A ₁ A ₃ B | 290.4 | 3.08 | 0.60±0.04 | 0.67 |
| | | | A ₁ A ₂ B | 180.6 | 3.26 | 0.14±0.06 | 0.38 |
| | | | A ₁ A ₂ A ₃ * | 69.6 | 0.96 | 0.22±0.06 | 0.00 |
| PG 1115+080 | optical, fold | 1.14 | A ₂ BC | 233.3 | 2.16 | 0.52±0.05 | 0.59 |
| | | | A ₁ BC | 218.8 | 2.43 | 0.76±0.03 | 0.70 |
| | | | A ₁ A ₂ C | 141.2 | 2.43 | 0.32±0.06 | 0.18 |
| | | | A ₁ A ₂ B | 126.7 | 1.86 | 0.10±0.06 | 0.06 |
| HST 12531–2914 | optical, cross | 0.54 | BCD | 172.4 | 1.04 | 0.39±0.05 | 0.37 |
| | | | ACD | 187.6 | 1.04 | 0.46±0.05 | 0.34 |
| | | | ABD | 206.8 | 1.36 | 0.31±0.06 | 0.49 |
| | | | ABC | 153.2 | 1.36 | 0.17±0.06 | 0.18 |
| HST 14113+5211 | optical, cross | 0.83 | BCD | 168.9 | 1.35 | 0.14±0.06 | 0.09 |
| | | | ACD | 161.3 | 2.28 | 0.36±0.05 | 0.42 |
| | | | ABD | 191.1 | 1.42 | 0.15±0.06 | 0.16 |
| | | | ABC | 198.7 | 2.28 | 0.67±0.03 | 0.63 |
| H1413+117 | near-IR, cross | 0.56 | BCD | 198.6 | 1.35 | 0.48±0.05 | 0.42 |
| | | | ACD | 186.2 | 1.10 | 0.37±0.05 | 0.47 |
| | | | ABD | 173.8 | 1.10 | 0.26±0.06 | 0.34 |
| | | | ABC | 161.4 | 1.35 | 0.24±0.06 | 0.13 |
| HST 14176+5226 | optical, cross | 1.33 | BCD | 172.8 | 2.36 | 0.04±0.06 | 0.03 |
| | | | ACD | 198.1 | 3.26 | 0.54±0.04 | 0.63 |
| | | | ABD | 187.2 | 2.36 | 0.13±0.06 | 0.08 |
| | | | ABC | 161.9 | 3.26 | 0.54±0.04 | 0.50 |
| B1422+231 | radio, cusp | 0.76 | BCD | 187.2 | 1.29 | 0.34±0.06 | 0.35 |
| | | | ACD | 283.0 | 1.29 | 0.96±0.01 | 0.94 |
| | | | ABD | 172.8 | 1.25 | 0.05±0.07 | 0.15 |
| | | | ABC* | 77.0 | 1.29 | 0.18±0.06 | 0.12 |

Table 1—Continued

| Lens | Type | R_{ein} (") | Triplet | θ (°) | d (") | R_{cusp} | |
|-----------|-------------------|----------------------|---------|--------------|---------|-------------------|-------|
| | | | | | | Data | Model |
| B1555+375 | radio, fold | 0.23 | BCD | 209.3 | 0.42 | 0.14 ± 0.07 | 0.55 |
| | | | ACD | 257.4 | 0.42 | 0.90 ± 0.01 | 0.88 |
| | | | ABD | 150.7 | 0.42 | 0.21 ± 0.06 | 0.03 |
| | | | ABC | 102.6 | 0.41 | 0.45 ± 0.05 | 0.14 |
| B1608+656 | radio, fold | 0.72 | BCD | 191.5 | 2.04 | 0.16 ± 0.06 | 0.07 |
| | | | ACD | 168.5 | 2.04 | 0.19 ± 0.06 | 0.24 |
| | | | ABD | 261.0 | 2.10 | 0.79 ± 0.02 | 0.89 |
| | | | ABC | 99.0 | 2.10 | 0.49 ± 0.05 | 0.49 |
| B1933+503 | radio, fold | 0.49 | 3,4,6 | 143.0 | 0.82 | 0.39 ± 0.05 | 0.01 |
| | | | 1,4,6 | 199.7 | 1.16 | 0.70 ± 0.03 | 0.63 |
| | | | 1,3,6 | 217.0 | 0.91 | 0.21 ± 0.06 | 0.29 |
| | | | 1,3,4 | 160.3 | 1.16 | 0.72 ± 0.03 | 0.42 |
| B2045+265 | radio, cusp | 1.13 | BCD | 183.9 | 1.93 | 0.05 ± 0.06 | 0.49 |
| | | | ACD | 325.1 | 1.93 | 0.88 ± 0.01 | 0.98 |
| | | | ABD | 176.1 | 1.92 | 0.21 ± 0.06 | 0.19 |
| | | | ACD* | 34.9 | 0.84 | 0.52 ± 0.04 | 0.02 |
| Q2237+030 | optical, cross | 0.85 | BCD | 186.5 | 1.65 | 0.29 ± 0.06 | 0.17 |
| | | | ACD | 173.5 | 1.65 | 0.20 ± 0.06 | 0.11 |
| | | | ABD | 146.2 | 1.83 | 0.71 ± 0.03 | 0.40 |
| | | | ABC | 213.8 | 1.83 | 0.52 ± 0.05 | 0.62 |

Note. — Data for image triplets in the 17 published 4-image lenses. The lens data are summarized by Turner et al. (2002). Column 2 gives the image configuration (fold, cusp, or cross) and indicates whether the flux ratios are measured at optical, near-IR, or radio wavelengths. The uncertainties in the observed values of R_{cusp} are obtained by assuming 10% uncertainties in the image fluxes; see §6 for more discussion. The predicted values of R_{cusp} are computed with the lens models given by Turner et al. (2002). For the cusp lenses B0712+472, RX J0911+0551, B1422+231, and B2045+265, the cusp image triplet is indicated by an *.

REFERENCES

Benson, A. J., Frenk, C. S., Lacey, C. G., Baugh, C. M., & Cole, S. 2002, MNRAS, 333, 177

Binney, J. J., & Evans, N. W. 2001, MNRAS, 327, L27

Bradač, M., Schneider, P., Steinmetz, M., Lombardi, M., King, L. J., & Porcas, R. 2002, A&A, 388, 373

Bullock, J. S., Kravtsov, A. V., & Weinberg, D. H. 2000, ApJ, 539, 517

Burud, I., et al. 1998, ApJ, 501, L5

Cardelli, J. A., Clayton, G. C., & Mathis, J. S. 1989, ApJ, 345, 245

Chang, K., & Refsdal, S. 1979, Nature, 282, 561

Chiba, M. 2002, ApJ, 565, 17

Cohn, J. D., Kochanek, C. S., McLeod, B. A., & Keeton, C. R. 2001, ApJ, 554, 1216

Dalal, N. 1998, ApJ, 509, L13

Dalal, N., & Rabin, J.M. 2001, J.Math.Phys., 42, 1818

Dalal, N., & Kochanek, C. S. 2002, ApJ, 572, 25

Debattista, V. P., & Sellwood, J. A. 2000, ApJ, 543, 704

de Blok, W. J. G., & Bosma, A. 2002, A&A, 385, 816

de Blok, W. J. G., McGaugh, S., & Rubin, V. 2001, AJ, 122, 2396

Evans, N. W., & Witt, H. 2001, MNRAS, 327, 1260

Evans, N. W., & Hunter, C. 2002, ApJ, 575, 68

Falco, E. E., Lehár, J., & Shapiro, I. I. 1997, AJ, 113, 540

Falco, E. E., Impey, C. D., Kochanek, C. S., Lehár, J., McLeod, B. A., Rix, H.-W., Keeton, C. R., Muñoz, J. A., & Peng, C. Y. 1999, ApJ, 523, 617

Fassnacht, C. D., et al. 1999, AJ, 117, 658

Flores, R. A., & Primack, J. R. 1994, ApJ, 427, L1

Font, A. S., Navarro, J. F., Stadel, J., & Quinn, T. 2001, ApJ, 563, L1

Gaudi, B. S., & Petters, A. O. 2002, ApJ, in press (preprint astro-ph/0206162)

Hall, P. B., Richards, G. T., York, D. G., Keeton, C. R., Bowen, D. V., Schneider, D. P., Schlegel, D. J., & Brinkmann, J. 2002, ApJ, 575, L51

Hayashi, E., Navarro, J. F., Taylor, J. E., Stadel, J., & Quinn, T. 2002, preprint (astro-ph/0203004)

Holder, G., & Schechter, P. 2002, preprint (astro-ph/0209532)

Hunter, C., & Evans, N. W. 2001, ApJ, 554, 1227

Irwin, M. J., Webster, R. L., Hewett, P. C., Corrigan, R. T., Jedrzejewski, R. I. 1989, AJ, 98, 1989

Jackson, N., et al. 1998, MNRAS, 296, 483

Jørgensen, I., Franx, M., & Kjærgaard, P. 1995, MNRAS, 273, 1097

Kassiola, A., & Kovner, I. 1993, ApJ, 417, 459

Keeton, C. R., Kochanek, C. S., & Seljak, U. 1997, ApJ, 482, 604

Keeton, C. R., & Kochanek, C. S. 1998, ApJ, 495, 157

Keeton, C. R., Kochanek, C. S., & Falco, E. E. 1998, ApJ, 509, 561

Keeton, C. R., Mao, S., & Witt, H. J. 2000, ApJ, 537, 697

Keeton, C. R. 2001a, ApJ, 561, 46

Keeton, C. R. 2001b, preprint (astro-ph/0102340)

Keeton, C. R. 2002a, ApJ, in press (preprint astro-ph/0206243)

Keeton, C. R. 2002b, ApJ, in press (preprint astro-ph/0111595)

Kent, S. M., & Falco, E. E. 1988, AJ, 96, 1570

Klypin, A., Kravtsov, A. V., Valenzuela, O., & Prada, F. 1999, ApJ, 522, 82

Kneib, J.-P., Cohen, J. G., & Hjorth, J. 2000, ApJ, 544, L35

Kochanek, C. S. 2002a, in Proc. Workshop, The Shapes of Galaxies and their Halos, ed. P. Natarjan (Singapore: World Scientific), 000 (also preprint astro-ph/0106495)

Kochanek, C. S. 2002b, preprint (astro-ph/0206006)

Koopmans, L. V. E., & Treu, T. 2002, preprint (astro-ph/0205281)

Kormann, R., Schneider, P., & Bartelmann, M. 1994, A&A, 284, 285

Mao, S., & Schneider, P. 1998, MNRAS, 295, 587

Metcalf, R. B., & Madau, P. 2001, ApJ, 563, 9

Metcalf, R. B., & Zhao, H. 2002, ApJ, 567, L5

Metcalf, R. B. 2002, preprint (astro-ph/0203012)

Moore, B. 1994, Nature, 370, 629

Moore, B., Ghigna, S., Governato, F., Lake, G., Quinn, T., Stadel, J., & Tozzi, P. 1999, ApJ, 524, L19

Moustakas, L. A., & Metcalf, R. B. 2002, preprint (astro-ph/0206176)

Paczyński, B. 1986, ApJ, 301, 503

Patnaik, A. R., & Narasimha, D. 2001, MNRAS, 326, 1403

Petters, A. O., Levine, H., & Wambsganss, J. 2001, Singularity Theory and Gravitational Lensing (Boston: Birkhäuser)

Rusin, D., & Tegmark, M. 2001, ApJ, 553, 709

Rusin, D., et al. 2001, *ApJ*, 557, 594

Schechter, P. L., & Wambsganss, J. 2002, *ApJ*, in press (preprint astro-ph/0204425)

Schneider, P., Ehlers, J., & Falco, E. E. 1992, *Gravitational Lenses* (Berlin: Springer)

Schneider, P., & Weiss, A. 1992, *A&A*, 260, 1

Sellwood, J. A. 2002, preprint (astro-ph/0210079)

Somerville, R. S. 2002, *ApJ*, 572, L23

Spergel, D. N., & Steinhardt, P. J. 2000, *PRL*, 84, 3760

Stoehr, F., White, S. D. M., Tormen, G., & Springel, V. 2002, *MNRAS*, in press (preprint astro-ph/0203342)

Sykes, C. M., et al. 1998, *MNRAS*, 301, 310

Turner, C., Keeton, C. R., & Kochanek, C. S. 2002, in preparation

Valenzuela, O., & Klypin, A. 2002, preprint (astro-ph/0204028)

van den Bosch, F. C., & Swaters, R. A. 2001, *MNRAS*, 325, 1017

Warren, S. J., Hewett, P. C., Lewis, G. F., Møller, P., Iovino, A., & Shaver, P. A. 1996, *MNRAS*, 278, 139

Warren, S. J., Lewis, G. F., Hewett, P. C., Møller, P., Shaver, P. A., & Iovino, A. 1999, *A&A*, 343, L35

Weinberg, M. D., & Katz, N. 2001, preprint (astro-ph/0110632)

Weiner, B. J., Sellwood, J. A., & Williams, T. B. 2001, *ApJ*, 546, 931

Winn, J. N., Hewitt, J. N., Patnaik, A. R., Schechter, P. L., Schommer, R. A., López, S., Maza, J., & Wachter, S. 2001, *AJ*, 121, 1223

Winn, J. N., Lovell, J. E. J., Chen, H.-W., Fletcher, A. B., Hewitt, J. N., Patnaik, A. R., & Schechter, P. L. 2002, *ApJ*, 564, 143

Witt, H. J., Mao, S., & Schechter, P. L. 1995, *ApJ*, 443, 18

Witt, H. J., & Mao, S. 2000, *MNRAS*, 311, 689

Zakharov, A. 1995, *A&A*, 293, 1

Zentner, A. R., & Bullock, J. S. 2002, *Phys. Rev. D*, 66, 043003

Zhao, H., & Pronk, D. 2001, *MNRAS*, 320, 401